

# Electrical control of valley-Zeeman spin-orbit coupling-induced spin precession at room temperature

Josep Ingla-Aynés,<sup>1,\*</sup> Franz Herling,<sup>1</sup> Jaroslav Fabian,<sup>2</sup> Luis E. Hueso,<sup>1,3</sup> and Fèlix Casanova<sup>1,3,†</sup>

<sup>1</sup>*CIC nanoGUNE BRTA, 20018 Donostia-San Sebastian, Basque Country, Spain*

<sup>2</sup>*Institute for Theoretical Physics, University of Regensburg, 93040 Regensburg, Germany*

<sup>3</sup>*IKERBASQUE, Basque Foundation for Science, 48013 Bilbao, Basque Country, Spain*

(Dated: June 29, 2021)

The ultimate goal of spintronics is achieving electrically controlled coherent manipulation of the electron spin at room temperature to enable devices such as spin field-effect transistors. With conventional materials, coherent spin precession has been observed in the ballistic regime and at low temperatures only. However, the strong spin anisotropy and the valley character of the electronic states in 2D materials provide unique control knobs to manipulate spin precession. Here, by manipulating the anisotropic spin-orbit coupling in bilayer graphene by the proximity effect to WSe<sub>2</sub>, we achieve coherent spin precession in the absence of an external magnetic field, even in the diffusive regime. Remarkably, the sign of the precessing spin polarization can be tuned by a back gate voltage and by a drift current. Our realization of a spin field-effect transistor at room temperature is a cornerstone for the implementation of energy efficient spin-based logic.

The realization of logic operations using the spin degree of freedom is a crucial goal for spintronics [1–5]. In this context, one of the most studied theoretical proposals is that of Datta and Das [6], which requires spin precession around the spin-orbit fields (SOFs) and has raised considerable interest [5–9]. However, the experimental achievement of the required strong spin-orbit coupling (SOC) regime in conventional materials can only be realized in ballistic systems with long momentum scattering time ( $\tau_p$ ) and very clean interfaces [7–9]. Consequently, its implementation in all-electrical devices is currently limited to low temperatures [10–15].

Alternatively, graphene-based van der Waals heterostructures are an ideal platform for spin manipulation [16, 17] since, in these systems, graphene’s low SOC can be enhanced by proximity with transition metal dichalcogenides (TMDs) [18–36]. Such graphene/TMD heterostructures possess a unique spin texture. In particular, the in-plane SOFs are of the Rashba type and point perpendicular to the electronic momentum. In the weak SOC regime, Rashba SOC caused by the stack inversion asymmetry leads to out-of-plane spin relaxation rates of  $(\tau_s^\perp)^{-1} = \Omega_R^2 \tau_p$ , where  $\Omega_R$  is the Larmor frequency around the Rashba SOFs. In contrast, the out-of-plane SOFs, which arise due to the broken sublattice symmetry in the TMD being imprinted on graphene, have opposite sign at the K and K’ valleys (see Fig. 1a) to preserve time reversal symmetry [18]. These SOFs, commonly called valley-Zeeman SOFs, give rise to spin-valley locking. In this case, the intervalley scattering time ( $\tau_{iv}$ ) is the characteristic time scale dominating the spin dynamics. Hence, in the weak SOC regime, the in-plane spin relaxation rate is given by  $(\tau_s^\parallel)^{-1} = \Omega_{VZ}^2 \tau_{iv} + (2\tau_s^\perp)^{-1}$ , where  $\Omega_{VZ}$  is the Larmor frequency around the valley-Zeeman SOFs. Since  $\tau_{iv}$  is typically much longer than  $\tau_p$  [37],  $\tau_{iv}\Omega_{VZ}$  becomes significantly bigger than  $\tau_p\Omega_R$  and, as a consequence, the spin transport is highly anisotropic

[23–27]. Unlike in conventional materials, the spin-valley locking present in graphene/TMD heterostructures might enable the strong SOC regime if  $\tau_{VZ}$  would become comparable to  $\tau_{iv}$ , where  $\tau_{VZ} = 2\pi/\Omega_{VZ}$  is the in-plane spin precession period around the out-of-plane valley-Zeeman SOFs (Fig. 1b). Such condition may even be achieved in the diffusive regime and could allow for room temperature operations.

In this Letter, we report the achievement of the strong SOC regime in bilayer graphene (BLG)/WSe<sub>2</sub> heterostructures, leading to magnetic-field free spin precession induced by the valley-Zeeman SOC as shown in Figs. 1a and 1b. Furthermore, by tuning the carrier density using a backgate voltage ( $V_{bg}$ ) and a drift current ( $I_{DC}$ ), we control the spin polarization up to room temperature, making our device operate as a Datta-Das spin field-effect transistor (see Figs. 1c and 1d). This hitherto unreported performance paves the way for the achievement of highly functional logic circuits [5, 38].

To measure SOC-induced spin precession, we prepared 2- $\mu\text{m}$ -wide (the heterostructure width is defined as  $W_{TMD}$  in Fig. 2a) BLG/WSe<sub>2</sub> lateral spin valves with spin-polarized TiO<sub>x</sub>/Co contacts and Ti/Au reference electrodes (Fig. 2a). BLG was chosen to take advantage of its gate tunable diffusivity. To ensure an efficient SOC and achieve the strong SOC regime, we chose WSe<sub>2</sub>, the TMD that imprints the largest valley-Zeeman SOC on graphene [18], and annealed the van der Waals heterostructures at 430°C. See Ref. [39] for the fabrication details, reproducibility, the role of the annealing temperature, and the role of  $W_{TMD}$  on the measured signals.

The diffusive spin transport experiments are performed in the nonlocal geometry (circuit in Fig. 2a, see Ref. [39] for measurement details). The  $y$ -spin accumulation ( $\mu_{sy}$ ) induced by applying a current  $I_{\delta 1}$  through contact 3 diffuses across the channel and builds a voltage difference  $V_{\delta 1} = P_d \mu_{sy}/e$  between contacts 4 and 7. Here  $P_d$  is

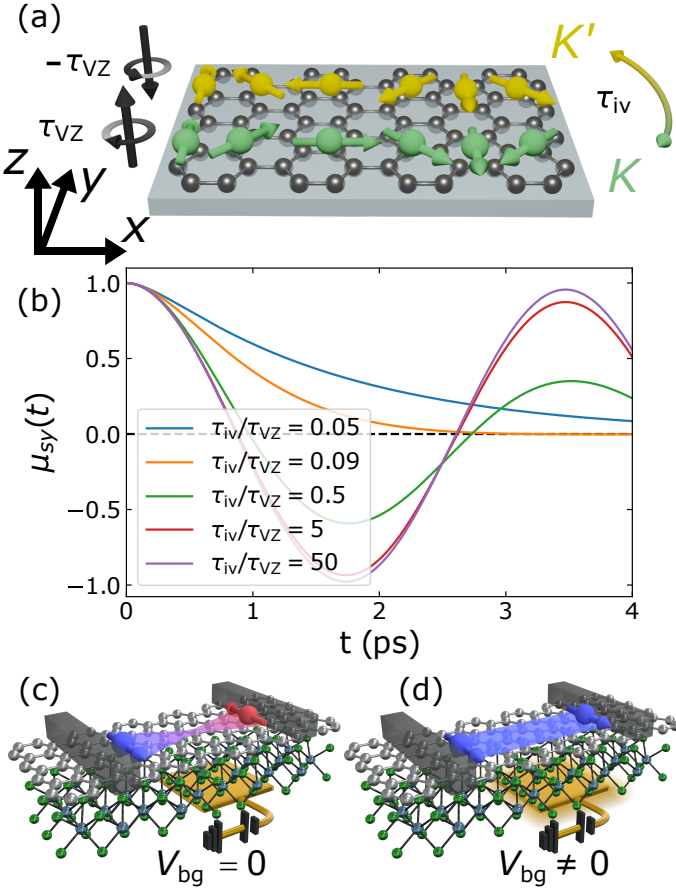


Figure 1. Device working principle and BLG/WSe<sub>2</sub> spin transistor operation. (a) Sketch of a BLG/WSe<sub>2</sub> heterostructure. Out-of-plane valley-Zeeman SOF (black arrows) with opposite sign at the K and K' valleys induce in-plane spin precession with a period  $\tau_{VZ}$ . Spins can scatter between the valleys via intervalley scattering ( $\tau_{IV}$ ). (b) Time dependence of the spin accumulation  $\mu_{sy}$  for different  $\tau_{IV}$  values (see Ref. [39] for details).  $\mu_{sy}$  undergoes net precession for  $\tau_{IV} \geq 0.5\tau_{VZ}$ . (c) and (d) Sketch of a spin field-effect transistor operating at the strong SOC regime where the valley-Zeeman induced spin precession is tuned by  $V_{bg}$  to control the sign reversal.

the detector spin polarization and  $e$  the electron charge. The nonlocal resistance ( $R_{nl} = V_{\delta 1}/I_{\delta 1}$ ) is measured as a function of a magnetic field applied along  $y$  ( $B_y$ ) in the conventional spin valve experiment. Figure 2b shows that, for  $V_{bg}=50$  V,  $R_{nl}$  in the antiparallel magnetization state ( $R_{nl}^{AP}$ ) is higher than in the parallel one ( $R_{nl}^P$ ). The spin signal, which is defined as  $\Delta R_{nl} = (R_{nl}^P - R_{nl}^{AP})/2$ , is thus negative. This observation could be a consequence of the sought in-plane spin precession induced by the valley-Zeeman coupling, although it could also be caused by the spin injector and detector having opposite spin polarizations [40, 41].

To confirm that  $\mu_{sy}$  is reversed during transport as in Fig. 1b, we induce out-of-plane spin precession by measuring  $R_{nl}$  as a function of a magnetic field applied along

$x$  ( $B_x$ ) (see Fig. 2c). In the parallel configuration,  $R_{nl}^P$  has a local maximum at  $B_x = 0$ , when the spins are not precessing. Then,  $R_{nl}^P$  decreases until it reaches a minimum *shoulder* ( $B_x \approx \pm 0.1$  T) when the average precession angle at the detector is of  $180^\circ$ . In this case, the spins injected along  $y$  cross the TMD-covered region pointing along  $z$ , and reach the detector pointing along  $-y$ . At higher  $B_x$ ,  $R_{nl}^P$  increases until it merges with  $R_{nl}^{AP}$  and  $\Delta R_{nl}$  reaches zero as the spins dephase and the contact magnetizations are pulled towards  $x$ . In contrast,  $R_{nl}^{AP}$  shows a minimum at  $B_x = 0$ , where it is higher than  $R_{nl}^P$ . As  $B_x$  increases,  $R_{nl}^{AP}$  also increases leading to an enhancement of  $\Delta R_{nl}$  with  $B_x$  (Fig. 2c, inset). This result is in stark contrast with standard spin precession measurements (where  $\Delta R_{nl}$  decreases at low  $B$ , until it reverses sign when the precessed angle is of  $90^\circ$  [24, 25]) and is a direct consequence of  $\mu_{sy}$  being reversed with respect to the out-of-plane spin accumulation. Finally,  $R_{nl}^{AP}$  reaches a maximum when the precessed angle at the detector is of  $180^\circ$ , before the contact magnetization pulling and spin dephasing decrease the spin signal until it vanishes for  $B_x > 0.2$  T. We observe that: (1) the magnitude of the in-plane spin signal ( $B_x = 0$ ) is significantly smaller than the out-of-plane one ( $B_x \approx \pm 0.1$  T), in agreement with previous works in graphene/TMD heterostructures [23–27]; (2) In contrast to the in-plane signal, the out-of-plane one is not reversed. This observation, together with the fact that out-of-plane spins are in the weak SOC regime [39], indicates that the sign reversal is not caused by the opposite sign of the injector and detector spin polarizations. Hence,  $\mu_{sy}$  must be reversed during transport. Spin transport experiments performed at the pristine BLG region show conventional positive signal for all  $V_{bg}$  values [39], evidencing that the sign reversal occurs across the TMD-covered region. Since the in-plane spin signal is negative without an applied magnetic field, we conclude that our experiments are probing the strong SOC regime. Note that our result provides the most direct experimental evidence that spin precession occurs between scattering events in graphene/TMD heterostructures [21–27].

In Fig. 2d (black curve), we plot the spin signal as a function of  $V_{bg}$ . The data shows that the signal is negative for  $V_{bg} > 20$  V and  $V_{bg} < -40$  V. For  $-40$  V  $< V_{bg} < 20$  V,  $\Delta R_{nl}$  is below the noise level (see Ref. [39] for the raw data). To understand the gate dependence, one must take into account the SOC in the BLG/WSe<sub>2</sub> heterostructure. As reported recently [28–30], the SOC in BLG/TMD heterostructures can have a pronounced electric field dependence. To obtain the  $V_{bg}$ -dependence of the SOC in our system, we have used the tight-binding Hamiltonian shown in Ref. [30] (see also Ref. [39]). To explain the symmetric dependence of  $\Delta R_{nl}$  vs  $V_{bg}$  with respect to the charge neutrality point, we have assumed that both layers have the same potential, which means that the externally applied field compensates for the in-

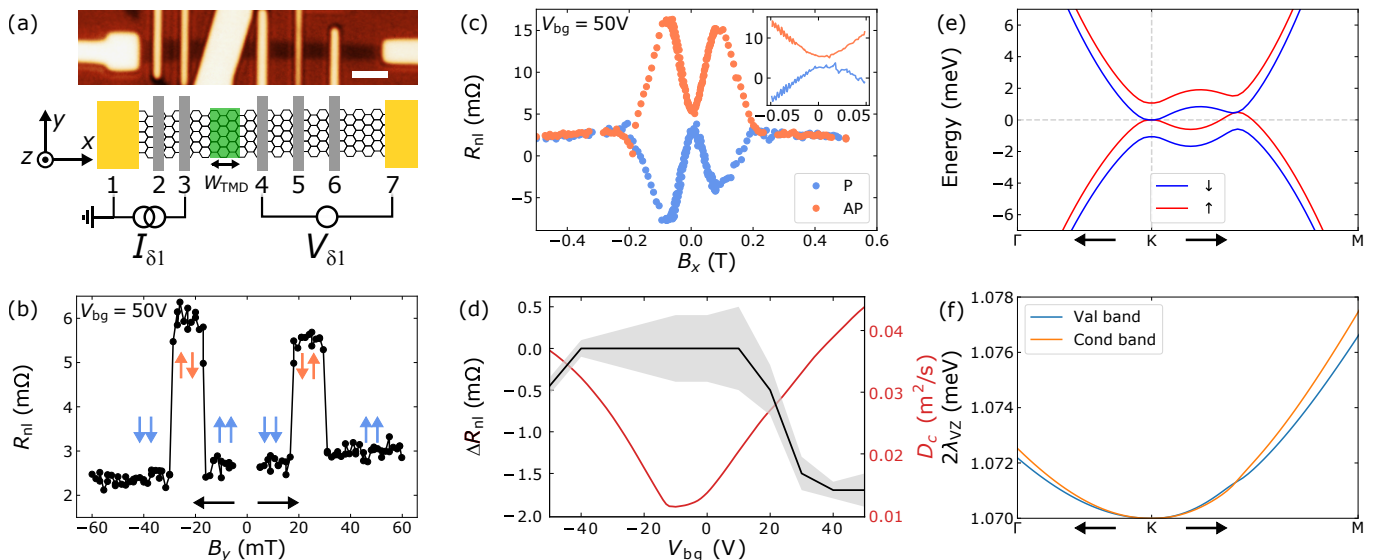


Figure 2. Diffusive spin transport at 50 K. (a) Optical image of the measured device. The BLG flake is the dark horizontal stripe and WSe<sub>2</sub> is the bright flake in the middle. The scale bar is 2 μm. The bottom panel shows a sketch of the device with the WSe<sub>2</sub>-covered BLG region shown in green. The circuit corresponds to the standard nonlocal spin diffusion measurement configuration. Contacts 1 and 7 are not magnetic (Ti/Au) and 2 to 6 are spin-polarized TiO<sub>x</sub>/Co contacts. (b) Nonlocal spin valve measurement across the WSe<sub>2</sub>-covered BLG region as a function of the magnetic field applied along  $y$  ( $B_y$ ) for  $V_{bg} = 50$  V. The horizontal arrows represent the  $B_y$ -sweep direction and the vertical ones the magnetization of contacts 3 and 4. (c) Nonlocal spin precession measurements with the magnetic field applied along  $x$  ( $B_x$ ) in the parallel (P) and anti-parallel (AP) configurations for  $V_{bg} = 50$  V. Inset: Low field detail. (d) Spin signal ( $\Delta R_{nl}$ ) and charge diffusivity ( $D_c$ ) as a function of  $V_{bg}$ . (e) Spin-polarized band structure of BLG/WSe<sub>2</sub> at zero electric field. The red lines represent spin-up (along  $+z$ ) and the blue ones spin-down (along  $-z$ ). (f) Spin splitting ( $2\lambda_{VZ}$ ) of the valence and conduction bands obtained from the band structure in panel e.

ternal 0.267 V/nm induced by the WSe<sub>2</sub> on the BLG at the charge neutrality point [28]. The results from this band-structure calculation are displayed in Figs. 2e and 2f and show perfect agreement with Ref. [28]. As expected, the conduction and valence bands cross at the K point because of the layer-symmetric configuration. Looking at the spin splitting ( $2\lambda_{VZ} = \hbar\Omega_{VZ}$ , where  $\hbar$  is the reduced Plank constant) in Fig. 2f, we observe that it depends very weakly with the energy, indicating that the proximity SOC remains almost constant through the calculated energy range. This observation implies that the  $V_{bg}$ -dependence of the SOC is unlikely to be the reason for the observed gate dependence. As shown in Fig. 1b and Ref. [39], if  $\tau_{iv}$  changes with  $V_{bg}$  [37], it can tune the spin precession frequency but, since proximitized graphene shows weak antilocalization [19–22], we could not measure weak localization in our device to extract  $\tau_{iv}$ . In contrast, the charge diffusivity ( $D_c$ ) of the BLG decreases significantly near the charge neutrality point (see red curve in Fig. 2d and Ref. [39]). As shown by our spin transport calculations [39], changes in  $D_s$  (which we obtain assuming  $D_s = D_c$  [42]), can have a crucial influence on the spin signal in the strong SOC regime, making  $D_s$  the most likely responsible for the measured  $V_{bg}$  dependence. However, the electron-hole asymmetry in  $\Delta R_{nl}$  indicates that other factors such as

spin absorption by the WSe<sub>2</sub> [43, 44] may also play a role. Note that we cannot discard a sign change of the signal below the noise level near the charge neutrality point.

By tuning the spin dynamics in the strong SOC regime, it should be possible to control the  $\Delta R_{nl}$  sign in a magnetic-field free device geometry. To confirm our hypothesis, we perform spin transport experiments under the effect of carrier drift in the geometry shown in Fig. 3a. The carrier drift is induced by  $I_{DC}$ , which is applied between contacts 4 and 1, and the spin current injected at contact 3 is detected as a nonlocal signal ( $R_{nl} = V_{\delta 2}/I_{\delta 2}$ ) between contacts 5 and 7. Since  $V_{\delta 2}$  is coupled to  $I_{\delta 2}$ , our measurement excludes the DC spin current injected by contact 4 [39]. The applied  $I_{DC}$  induces a drift velocity  $v_d = I_{DC}/(W_{BLG}ne)$ , where  $n$  is the carrier density in the channel and  $W_{BLG}$  is the BLG flake width. The induced  $v_d$  changes the spin transport time across the BLG/WSe<sub>2</sub> [45–47], leading to a tuning of the spatial oscillation frequency of  $\mu_{sy}$  [39]. In Fig. 3b, we present spin valve measurements at  $V_{bg} = -50$  V and  $I_{DC} = -40, 0, \text{ and } 40 \mu\text{A}$ . We observe that, in contrast with the results obtained from spin drift experiments in the pristine graphene region [39],  $\Delta R_{nl}$  reverses sign as we sweep  $I_{DC}$  from  $-40$  to  $40 \mu\text{A}$ , and becomes smaller than the noise level for  $I_{DC} = 0$ . This result is the first demonstration of carrier drift-control of spin reversal in an all-electrical de-

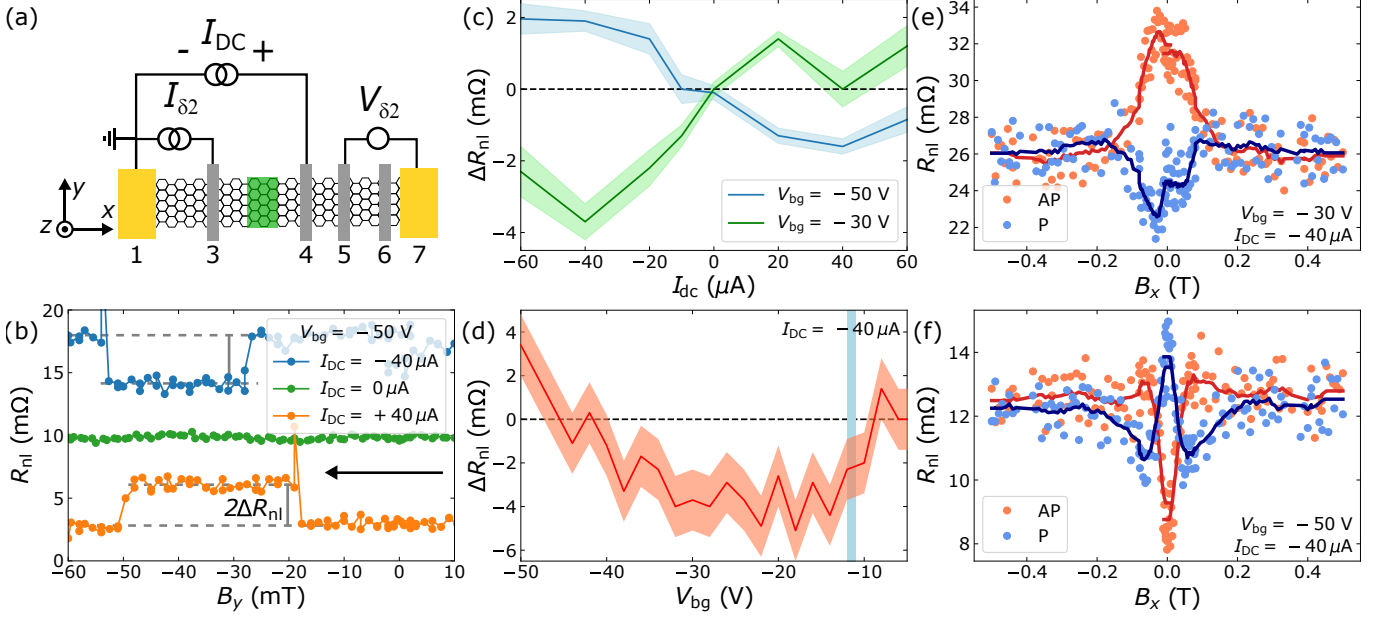


Figure 3. Controlling spin transport with drift at 50 K. (a) Sketch of the device with the spin drift measurement configuration. (b) Nonlocal spin valve measurements for  $V_{bg} = -50$  V at  $I_{DC} = -40, 0,$  and  $+40$   $\mu\text{A}$ . The curves have been shifted for clarity. (c)  $I_{DC}$ -dependence of  $\Delta R_{nl}$  at  $V_{bg} = -50$  and  $-30$  V. (d)  $\Delta R_{nl}$  vs  $V_{bg}$  at  $I_{DC} = -40$   $\mu\text{A}$ . The vertical light blue line is the charge neutrality point of the WSe<sub>2</sub>-covered BLG region. (e), (f) Nonlocal spin precession measurements with  $B_x$  in the P and AP configurations for  $I_{DC} = -40$   $\mu\text{A}$  and  $V_{bg} = -30$  V and  $-50$  V, respectively. The lines are obtained by averaging over a window of eleven points.

vice. Such unprecedented observation is consistent with the spin transport model shown in Figs. 1a and 1b if the in-plane spin precession angle at  $I_{DC}=0$  is a multiple of  $90^\circ$  (see Ref. [39] for more detailed calculations). A comprehensive illustration of this behavior is shown in Fig. 3c, where we plot  $\Delta R_{nl}$  vs  $I_{DC}$  as extracted from spin valve measurements performed at  $V_{bg} = -50$  and  $-30$  V (see Ref. [39] for the complete set of data). Importantly, we find that  $\Delta R_{nl}$  reverses sign between the two  $V_{bg}$  for all the  $I_{DC}$  values. To explain this sign reversal, we consider  $\lambda_{VZ}$ ,  $\tau_{iv}$ , and  $D_s$ , that are the relevant parameters that could change with  $V_{bg}$  (note that  $\tau_s^\perp$  and  $n$ , that changes  $v_d$ , cannot explain the observed sign reversal, see Ref. [39] for details). We dismiss  $\lambda_{VZ}$  because, according to our tight-binding calculations (Figs. 2e and 2f), the valley-Zeeman SOC does not have a significant dependence with  $V_{bg}$ . As mentioned above,  $\tau_{iv}$  may change with  $V_{bg}$  [37] and modify the effective spin precession frequency, as shown in Fig. 1b and [39]. Finally, we consider the change in  $D_s$  from 0.01 to 0.03  $\text{m}^2/\text{s}$  and observe that it has a strong influence on the  $\mu_{sy}$  spatial frequency [39]. Even though both  $\tau_{iv}$  and  $D_s$  could be responsible for the sign reversal of  $\Delta R_{nl}$  with  $V_{bg}$ , the extracted change in  $D_s$  is large enough to explain a sign reversal keeping  $\tau_{iv}$  constant.

Our observation of a sign reversal in  $\Delta R_{nl}$  with  $V_{bg}$  at fixed  $I_{DC}$  is very promising for Datta-Das spin field-effect transistor operations which work in the diffusive

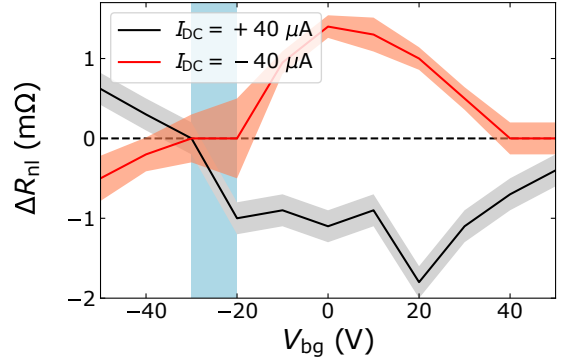


Figure 4. Room temperature electrical control of spin transport.  $V_{bg}$ -dependence of  $\Delta R_{nl}$  for  $I_{DC} = \pm 40$   $\mu\text{A}$ . The blue area represents the charge neutrality point of the WSe<sub>2</sub>-covered BLG region. As at 50 K,  $\Delta R_{nl}$  reverses sign upon changing the sign of  $I_{DC}$ .

regime, as sketched in Figs. 1c and 1d. In Fig. 3d, we plot  $\Delta R_{nl}$  vs  $V_{bg}$  at  $I_{DC} = -40$   $\mu\text{A}$ . We find that  $\Delta R_{nl}$  becomes positive for  $V_{bg} < -45$  V and at  $V_{bg} = -8$  V.

Finally, we measure spin precession around  $B_x$  to confirm that the out-of-plane spin signal has not changed sign and the previous results are indeed caused by in-plane spin precession. The results are shown in Figs. 3e and 3f for  $V_{bg} = -30$  and  $-50$  V, respectively. For  $V_{bg} = -30$  V, the spin precession data looks similar to the one in Fig. 2c with the difference that the in-plane

$B_x = 0$  signal in Fig. 3e is comparable to the maximum signal at the shoulders. As a consequence, the shoulders are less clear than in Fig. 2c. In contrast, the  $R_{nl}$  vs  $B_x$  data at  $V_{bg} = -50$  V shows a conventional spin precession shape where the in-plane spin signal is positive and larger than  $\Delta R_{nl}$  at the shoulders, more similar to isotropic systems [24, 25]. See Ref [39] for the evolution of the spin precession data with  $I_{DC}$ .

To confirm that the measured effect is suitable for applications, we perform spin valve experiments at 300 K as a function of  $V_{bg}$  (see Ref. [39] for the raw data). The  $\Delta R_{nl}$  values are plotted in Fig. 4 for  $I_{DC} = \pm 40 \mu A$ . These results are very similar to those at 50 K, demonstrating that our device is in the strong SOC regime up to room temperature and the spin orientation can be controlled using both  $I_{DC}$  and  $V_{bg}$ . Similar results obtained in a second sample are shown in Ref. [39].

To conclude, we demonstrate the valley-Zeeman SOC induced magnetic-field free control of spin precession in a BLG/WSe<sub>2</sub> van der Waals heterostructure at the strong SOC regime. By tuning the carrier density using  $V_{bg}$  and  $I_{DC}$ , we control the spin polarization up to room temperature, making our device operate as a spin field-effect transistor. This achievement has prospect for future spin-based logic applications such as nonvolatile and reconfigurable logic [38] and as a complement to the existing spin-logic proposals [1–4].

## ACKNOWLEDGMENTS

We acknowledge R. Llopis and R. Gay for technical assistance and C. K. Safer, N. Ontoso, and K. Zollner for discussions. This work is supported by the Spanish MICINN under the Maria de Maeztu Units of Excellence Programme (MDM-2016-0618) under Project RTI2018-094861-B-100 and by the the European Union H2020 under the Marie Skłodowska Curie Actions (0766025-QuESTech). J. F. acknowledges Deutsche Forschungsgemeinschaft (DFG, German Research Foundation) SFB1277 (Project-ID 314695032), SPP 2244, and the European Unions Horizon 2020 research and innovation program under Grant No. 785219. J.I.-A. acknowledges postdoctoral fellowship support from the “Juan de la Cierva - Formación” program by the Spanish MICINN (Grant No. FJC2018-038688-I).

\* j.ingla@nanogune.eu

† f.casanova@nanogune.eu

[1] H. Dery, P. Dalal, L. Sham, *et al.*, Spin-based logic in semiconductors for reconfigurable large-scale circuits, *Nature* **447**, 573 (2007).

- [2] B. Behin-Aein, D. Datta, S. Salahuddin, and S. Datta, Proposal for an all-spin logic device with built-in memory, *Nat. Nanotechnol.* **5**, 266 (2010).
- [3] S. Manipatruni, D. E. Nikonov, C.-C. Lin, T. A. Gosavi, H. Liu, B. Prasad, Y.-L. Huang, E. Bonturim, R. Ramesh, and I. A. Young, Scalable energy-efficient magnetoelectric spin-orbit logic, *Nature* **565**, 35 (2019).
- [4] V. T. Pham, I. Groen, S. Manipatruni, W. Y. Choi, D. E. Nikonov, E. Sagasta, C.-C. Lin, T. A. Gosavi, A. Marty, L. E. Hueso, I. A. Young, *et al.*, Spin-orbit magnetic state readout in scaled ferromagnetic/heavy metal nanostructures, *Nat. Elec.* **3**, 309 (2020).
- [5] B. Dieny, I. L. Prejbeanu, K. Garello, P. Gambardella, P. Freitas, R. Lehdorff, W. Raberg, U. Ebels, S. O. Demokritov, J. Akerman, *et al.*, Opportunities and challenges for spintronics in the microelectronics industry, *Nature Electronics* **3**, 446 (2020).
- [6] S. Datta and B. Das, Electronic analog of the electro-optic modulator, *Appl. Phys. Lett.* **56**, 665 (1990).
- [7] I. Žutić, J. Fabian, and S. Das Sarma, Spintronics: Fundamentals and applications, *Rev. Mod. Phys.* **76**, 323 (2004).
- [8] J. Schliemann, J. C. Egues, and D. Loss, Nonballistic spin-field-effect transistor, *Phys. Rev. Lett.* **90**, 146801 (2003).
- [9] X. Liu, X.-J. Liu, and J. Sinova, Spin dynamics in the strong spin-orbit coupling regime, *Phys. Rev. B* **84**, 035318 (2011).
- [10] H. C. Koo, J. H. Kwon, J. Eom, J. Chang, S. H. Han, and M. Johnson, Control of spin precession in a spin-injected field effect transistor, *Science* **325**, 1515 (2009).
- [11] J. Wunderlich, B.-G. Park, A. C. Irvine, L. P. Zárbo, E. Rozkotová, P. Nemeč, V. Novák, J. Sinova, and T. Jungwirth, Spin hall effect transistor, *Science* **330**, 1801 (2010).
- [12] K. Olejník, J. Wunderlich, A. Irvine, R. Campion, V. Amin, J. Sinova, and T. Jungwirth, Detection of electrically modulated inverse spin hall effect in an fe/gaas microdevice, *Phys. Rev. Lett.* **109**, 076601 (2012).
- [13] C. Pojen, H. Sheng-Chin, L. W. Smith, F. Sfigakis, M. Pepper, C. Chin-Hung, F. Ju-Chun, J. P. Griffiths, I. Farrer, H. E. Beere, G. A. C. Jones, D. A. Ritchie, and T.-M. Chen, All-electric all-semiconductor spin field-effect transistors, *Nat. Nanotechnol.* **10**, 35 (2015).
- [14] W. Y. Choi, H.-j. Kim, J. Chang, S. H. Han, H. C. Koo, and M. Johnson, Electrical detection of coherent spin precession using the ballistic intrinsic spin hall effect, *Nat. Nanotechnol.* **10**, 666 (2015).
- [15] W. Y. Choi, H.-j. Kim, J. Chang, S. H. Han, A. Abbout, H. B. M. Saidaoui, A. Manchon, K.-J. Lee, and H. C. Koo, Ferromagnet-free all-electric spin hall transistors, *Nano Lett.* **18**, 7998 (2018).
- [16] W. Han, R. K. Kawakami, M. Gmitra, and J. Fabian, Graphene spintronics, *Nat. Nanotechnol.* **9**, 794 (2014).
- [17] J. H. Garcia, M. Vila, A. W. Cummings, and S. Roche, Spin transport in graphene/transition metal dichalcogenide heterostructures, *Chem. Soc. Rev.* **47**, 3359 (2018).
- [18] M. Gmitra, D. Kochan, P. Högl, and J. Fabian, Trivial and inverted dirac bands and the emergence of quantum spin hall states in graphene on transition-metal dichalcogenides, *Phys. Rev. B* **93**, 155104 (2016).
- [19] Z. Wang, D.-K. Ki, J. Y. Khoo, D. Mauro, H. Berger, L. S. Levitov, and A. F. Morpurgo, Origin and magni-

- tude of ‘designer’ spin-orbit interaction in graphene on semiconducting transition metal dichalcogenides, *Phys. Rev. X* **6**, 041020 (2016).
- [20] B. Yang, M.-F. Tu, J. Kim, Y. Wu, H. Wang, J. Alicea, R. Wu, M. Bockrath, and J. Shi, Tunable spin-orbit coupling and symmetry-protected edge states in graphene/ws2, *2D Mater.* **3**, 031012 (2016).
- [21] S. Zihlmann, A. W. Cummings, J. H. Garcia, M. Kedves, K. Watanabe, T. Taniguchi, C. Schönnenberger, and P. Makk, Large spin relaxation anisotropy and valley-zeeman spin-orbit coupling in wse2/graphene/h-bn heterostructures, *Phys. Rev. B* **97**, 075434 (2018).
- [22] T. Wakamura, F. Reale, P. Palczynski, S. Guéron, C. Mattevi, and H. Bouchiat, Strong anisotropic spin-orbit interaction induced in graphene by monolayer ws2, *Phys. Rev. Lett.* **120**, 106802 (2018).
- [23] A. W. Cummings, J. H. Garcia, J. Fabian, and S. Roche, Giant spin lifetime anisotropy in graphene induced by proximity effects, *Phys. Rev. Lett.* **119**, 206601 (2017).
- [24] T. S. Ghiasi, J. Ingla-Aynés, A. A. Kaverzin, and B. J. van Wees, Large proximity-induced spin lifetime anisotropy in transition-metal dichalcogenide/graphene heterostructures, *Nano Lett.* **17**, 7528 (2017).
- [25] L. A. Benítez, J. F. Sierra, W. Saverio Torres, A. Arrighi, F. Bonell, M. V. Costache, and S. O. Valenzuela, Strongly anisotropic spin relaxation in graphene–transition metal dichalcogenide heterostructures at room temperature, *Nat. Phys.* **14**, 303 (2018).
- [26] S. Omar, B. N. Madhushankar, and B. J. van Wees, Large spin-relaxation anisotropy in bilayer-graphene/WS<sub>2</sub> heterostructures, *Phys. Rev. B* **100**, 155415 (2019).
- [27] M. Offidani and A. Ferreira, Microscopic theory of spin relaxation anisotropy in graphene with proximity-induced spin-orbit coupling, *Phys. Rev. B* **98**, 245408 (2018).
- [28] M. Gmitra and J. Fabian, Proximity Effects in Bilayer Graphene on Monolayer WSe<sub>2</sub>: Field-Effect Spin Valley Locking, Spin-Orbit Valve, and Spin Transistor, *Phys. Rev. Lett.* **119**, 146401 (2017).
- [29] J. Y. Khoo, A. F. Morpurgo, and L. Levitov, On-demand spin-orbit interaction from which-layer tunability in bilayer graphene, *Nano Lett.* **17**, 7003 (2017).
- [30] K. Zollner, M. Gmitra, and J. Fabian, Swapping exchange and spin-orbit coupling in 2d van der waals heterostructures, *Phys. Rev. Lett.* **125**, 196402 (2020).
- [31] Y. K. Luo, J. Xu, T. Zhu, G. Wu, E. J. McCormick, W. Zhan, M. R. Neupane, and R. K. Kawakami, Opto-valleytronic spin injection in monolayer mos2/few-layer graphene hybrid spin valves, *Nano Lett.* **17**, 3877 (2017).
- [32] A. Avsar, D. Unuchek, J. Liu, O. L. Sanchez, K. Watanabe, T. Taniguchi, B. Ozyilmaz, and A. Kis, Optospintronics in graphene via proximity coupling, *ACS Nano* **11**, 11678 (2017).
- [33] J. Island, X. Cui, C. Lewandowski, J. Khoo, E. Spanton, H. Zhou, D. Rhodes, J. Hone, T. Taniguchi, K. Watanabe, *et al.*, Spin-orbit-driven band inversion in bilayer graphene by the van der waals proximity effect, *Nature* **571**, 85 (2019).
- [34] C. Safeer, J. Ingla-Aynés, F. Herling, J. H. Garcia, M. Vila, N. Ontoso, M. R. Calvo, S. Roche, L. E. Hueso, and F. Casanova, Room-temperature spin Hall effect in graphene/MoS<sub>2</sub> van der Waals heterostructures, *Nano Lett.* **19**, 1074 (2019).
- [35] T. S. Ghiasi, A. A. Kaverzin, P. J. Blah, and B. J. van Wees, Charge-to-spin conversion by the rashba–edelstein effect in two-dimensional van der waals heterostructures up to room temperature, *Nano Lett.* **19**, 5959 (2019).
- [36] L. A. Benítez, W. S. Torres, J. F. Sierra, M. Timmermans, J. H. Garcia, S. Roche, M. V. Costache, and S. O. Valenzuela, Tunable room-temperature spin galvanic and spin hall effects in van der waals heterostructures, *Nat. Mater.* **19**, 170 (2020).
- [37] R. Gorbachev, F. Tikhonenko, A. Mayorov, D. Horsell, and A. Savchenko, Weak localization in bilayer graphene, *Phys. Rev. Lett.* **98**, 176805 (2007).
- [38] S. Sugahara and J. Nitta, Spin-transistor electronics: An overview and outlook, *Proceedings of the IEEE* **98**, 2124 (2010).
- [39] See Supplemental Material for sample fabrication, measurement details, additional measurements, and modeling details.
- [40] M. V. Kamalakar, A. Dankert, P. J. Kelly, and S. P. Dash, Inversion of spin signal and spin filtering in ferromagnet—hexagonal boron nitride-graphene van der waals heterostructures, *Scientific Reports* **6**, 1 (2016).
- [41] J. Xu, S. Singh, J. Katoch, G. Wu, T. Zhu, I. Žutić, and R. K. Kawakami, Spin inversion in graphene spin valves by gate-tunable magnetic proximity effect at one-dimensional contacts, *Nat. Commun.* **9**, 1 (2018).
- [42] T. Maassen, F. Dejene, M. Guimarães, C. Józsa, and B. Van Wees, Comparison between charge and spin transport in few-layer graphene, *Phys. Rev. B* **83**, 115410 (2011).
- [43] W. Yan, O. Txoperena, R. Llopis, H. Dery, L. E. Hueso, and F. Casanova, A two-dimensional spin field-effect switch, *Nat. Commun.* **7**, 13372 (2016).
- [44] A. Dankert and S. P. Dash, Electrical gate control of spin current in van der waals heterostructures at room temperature, *Nat. Commun.* **8**, 16093 (2017).
- [45] Z. G. Yu and M. E. Flatté, Spin diffusion and injection in semiconductor structures: Electric field effects, *Phys. Rev. B* **66**, 235302 (2002).
- [46] C. Józsa, M. Popinciuc, N. Tombros, H. T. Jonkman, and B. J. van Wees, Electronic spin drift in graphene field-effect transistors, *Phys. Rev. Lett.* **100**, 236603 (2008).
- [47] J. Ingla-Aynés, R. J. Meijerink, and B. J. van Wees, Eighty-eight percent directional guiding of spin currents with 90  $\mu\text{m}$  relaxation length in bilayer graphene using carrier drift, *Nano Lett.* **16**, 4825 (2016).
- [48] A. Castellanos-Gomez, M. Buscema, R. Molenaar, V. Singh, L. Janssen, H. S. Van Der Zant, and G. A. Steele, Deterministic transfer of two-dimensional materials by all-dry viscoelastic stamping, *2D Mater.* **1**, 011002 (2014).
- [49] K. S. Novoselov, A. K. Geim, S. V. Morozov, D. Jiang, Y. Zhang, S. V. Dubonos, I. V. Grigorieva, and A. A. Firsov, Electric field effect in atomically thin carbon films, *Science* **306**, 666 (2004).
- [50] E. McCann and M. Koshino, The electronic properties of bilayer graphene, *Rep. Prog. Phys.* **76**, 056503 (2013).
- [51] Y. Zhang, T.-T. Tang, C. Girit, Z. Hao, M. C. Martin, A. Zettl, M. F. Crommie, Y. R. Shen, and F. Wang, Direct observation of a widely tunable bandgap in bilayer graphene, *Nature* **459**, 820 (2009).
- [52] D. Bandurin, I. Torre, R. K. Kumar, M. B. Shalom, A. Tomadin, A. Principi, G. Auton, E. Khestanova, K. Novoselov, I. Grigorieva, *et al.*, Negative local resis-

- tance caused by viscous electron backflow in graphene, *Science* **351**, 1055 (2016).
- [53] Y. Li and M. Koshino, Twist-angle dependence of the proximity spin-orbit coupling in graphene on transition-metal dichalcogenides, *Phys. Rev. B* **99**, 075438 (2019).
- [54] A. David, P. Rakyta, A. Kormányos, and G. Burkard, Induced spin-orbit coupling in twisted graphene–transition metal dichalcogenide heterobilayers: Twistronics meets spintronics, *Phys. Rev. B* **100**, 085412 (2019).
- [55] T. Maassen, I. Vera-Marun, M. Guimarães, and B. Van Wees, Contact-induced spin relaxation in hane spin precession measurements, *Phys. Rev. B* **86**, 235408 (2012).
- [56] H. Idzuchi, A. Fert, and Y. Otani, Revisiting the measurement of the spin relaxation time in graphene-based devices, *Phys. Rev. B* **91**, 241407 (2015).
- [57] D. Purdie, N. Pugno, T. Taniguchi, K. Watanabe, A. Ferrari, and A. Lombardo, Cleaning interfaces in layered materials heterostructures, *Nat. Commun.* **9**, 1 (2018).
- [58] F. Herling, C. Safeer, J. Ingla-Aynés, N. Ontoso, L. E. Hueso, and F. Casanova, Gate tunability of highly efficient spin-to-charge conversion by spin Hall effect in graphene proximitized with WSe<sub>2</sub>, *APL Mater.* **8**, 071103 (2020).
- [59] J. C. Leutenantsmeyer, J. Ingla-Aynés, J. Fabian, and B. J. van Wees, Observation of spin-valley-coupling-induced large spin-lifetime anisotropy in bilayer graphene, *Phys. Rev. Lett.* **121**, 127702 (2018).
- [60] Z. Yue, K. Tian, A. Tiwari, and M. Raikh, Spin transport in n-type single-layer transition-metal dichalcogenides, *Phys. Rev. B* **93**, 195301 (2016).
- [61] W. Han, J.-R. Chen, D. Wang, K. M. McCreary, H. Wen, A. G. Swartz, J. Shi, and R. K. Kawakami, Spin relaxation in single-layer graphene with tunable mobility, *Nano Lett.* **12**, 3443 (2012).
- [62] S. Konschuh, M. Gmitra, D. Kochan, and J. Fabian, Theory of spin-orbit coupling in bilayer graphene, *Phys. Rev. B* **85**, 115423 (2012).

**Supplemental Material of "Electrical control of valley-Zeeman spin-orbit coupling-induced spin precession at room temperature"**

## CONTENTS

Acknowledgments	5
References	5
Device fabrication	3
Electronic measurements	3
Analysis of the $V_{bg}$ sweeps	3
Measurement of the square resistance of the pristine and WSe <sub>2</sub> -covered BLG regions	3
Determination of the charge diffusivity	4
Determination of the momentum scattering time and the Rashba SOC period	5
Spin transport at the pristine graphene region at 50 K	6
Spin transport across the WSe <sub>2</sub> -covered graphene region at 50 K	7
Spin drift experiments across the WSe <sub>2</sub> -covered region at 50 K	7
Spin drift experiments across the WSe <sub>2</sub> -covered region at 300 K	10
Spin drift experiments at the pristine graphene region at 300 K	13
Reproducibility	13
Influence of the annealing temperature and WSe <sub>2</sub> width on the proximity-induced SOC	14
Modeling details	16
Weak SOC regime	16
Strong SOC regime	17
$I_{DC}$ -dependence of $\Delta R_{nl}$ .	18
Influence of the charged impurities on spin transport in the strong SOC regime	19
Tight binding calculations	19
Effect of a perpendicular electric field on the spin texture of bilayer graphene	20

## DEVICE FABRICATION

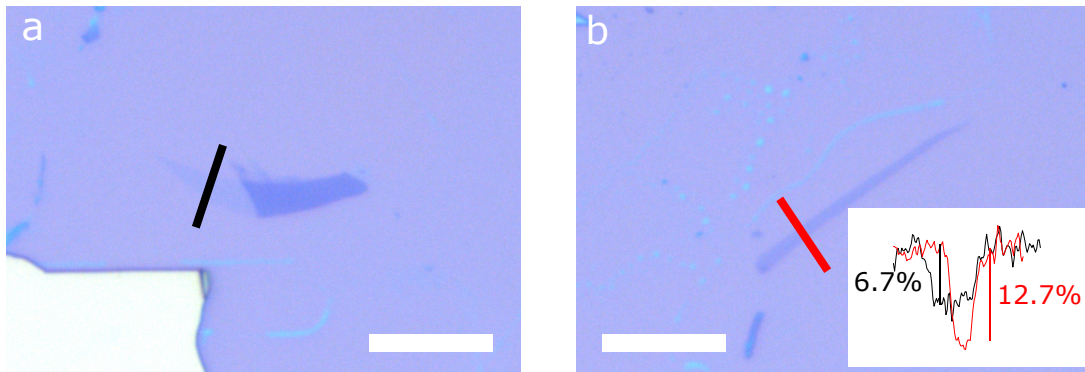


Figure S1. Optical contrast of BLG. (a) Optical microscope image of a monolayer graphene flake. (b) Optical microscope image of the BLG flake used to prepare the device shown in the main text. Inset: Intensity profiles taken along the black and red lines with the respective colors. The optical contrast of the monolayer is 6.7% and the bilayer 12.7%. The scale bars are 10  $\mu\text{m}$ .

The BLG flake was obtained by cleaving a highly oriented pyrolytic graphite crystal (provided by HQ graphene) on a Si substrate with 300 nm of thermal oxide using Nitto SPV 224P tape. To realize spin transport in a channel with tuneable diffusivity, we select bilayer graphene (BLG) as the optimal channel material. To determine the number of layers of the exfoliated flakes, we used optical contrast. In particular, the optical contrast of BLG is twice the one of monolayer graphene (see Fig. S1). The  $\text{WSe}_2$  was exfoliated from a crystal (by HQ graphene) on a PDMS stamp (gelpack 4). The 27-nm-thick  $\text{WSe}_2$  flake was transferred on top of the graphene flake using the viscoelastic stamping technique [48] and the resulting heterostructure was annealed for 1 h at 430  $^\circ\text{C}$  under high vacuum conditions. Next, we prepared the Ti(5 nm)/Au(35 nm) contacts using standard e-beam lithography, e-beam deposition of Ti and thermal deposition of Au. Finally, after being defined by e-beam lithography, the  $\text{TiO}_x/\text{Co}$  contacts were prepared by depositing 3  $\text{\AA}$  of Ti and, after oxidation in ambient conditions, 35 nm of Co were deposited by e-beam evaporation. Finally, 5 nm of Au were deposited to cap the Co layer, and the whole structure was covered by an insulating hexagonal boron nitride flake. Figure S2a shows an optical micrograph image of the device before the electronic measurements.

## ELECTRONIC MEASUREMENTS

The spin (charge) transport measurements were performed using the DC reversal ( $\delta$ ) mode of a Keithley 6221 current source and a Keithley 2182 nanovoltmeter with a delay of 20 ms and an excitation current of  $I_{\delta 1(2)} = 80 \mu\text{A}$  ( $1 \mu\text{A}$  for charge transport). The DC reversal technique allows us to measure small signals while removing backgrounds, enabling for the measurement of the nonlocal spin signal  $V_{\delta 1}$  in the circuit of Fig. 2a of the main manuscript. Furthermore, the DC reversal technique also allows us to remove the DC spins injected by contact 4 in the drift current geometry shown in Fig. 3a of the main manuscript. Additionally, the carrier density of the graphene channel is tuned by applying a  $V_{\text{bg}}$  to the doped Si substrate (see Section S2). Both  $I_{\text{DC}}$  and  $V_{\text{bg}}$  are applied using a Keithley 2636B system source meter. The magnetic field is applied using a superconducting solenoid and a rotator to orient magnetic fields along the  $x$  and  $y$  directions defined in Fig. 2a of the main manuscript.

## ANALYSIS OF THE $V_{\text{bg}}$ SWEEPS

### Measurement of the square resistance of the pristine and $\text{WSe}_2$ -covered BLG regions

To determine the charge transport properties of the different regions of the device shown in the main manuscript and Fig. S2, we measured the channel's square resistance  $R_{\text{sq}}$  as a function of the backgate voltage ( $V_{\text{bg}}$ ), that is applied to the doped Si substrate [49]. The  $V_{\text{bg}}$  controls the carrier density ( $n$ ) in the graphene channel via the field effect,

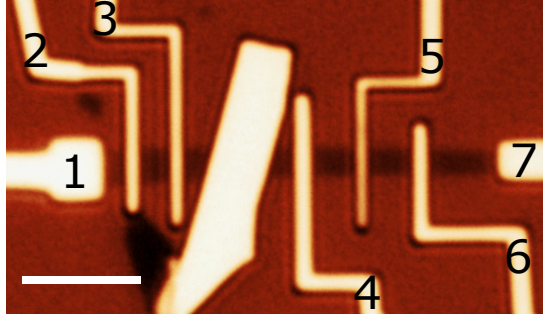


Figure S2. Optical microscope image of the device with the corresponding contact numbering. The scale bar is 4  $\mu\text{m}$ .

TABLE I. Geometrical device parameters.

$W_{\text{gr}}^{43}$ ( $\mu\text{m}$ )	$L_{43}$ ( $\mu\text{m}$ )	$W_{\text{gr}}^{54}$ ( $\mu\text{m}$ )	$L_{54}$ ( $\mu\text{m}$ )	$W_{\text{TMD}}$ ( $\mu\text{m}$ )
0.85	4.30	0.80	2.00	2.00

$$n = \frac{\epsilon_0 \epsilon_r}{et_{\text{SiO}_2}} (V_{\text{bg}} - V_{\text{cnp}}), \quad (\text{S1})$$

where  $\epsilon_0$  is the vacuum dielectric permittivity,  $\epsilon_r = 3.9$  is the dielectric constant of  $\text{SiO}_2$ ,  $e$  the electron charge,  $t_{\text{SiO}_2} = 300 \text{ nm}$  is the thickness of the  $\text{SiO}_2$  dielectric, and  $V_{\text{cnp}}$  the value of  $V_{\text{bg}}$  at which the graphene reaches the charge neutrality point (CNP). In Fig. S3a, we show  $R_{\text{sq}}$  vs  $V_{\text{bg}}$  at the pristine graphene region ( $R_{\text{sq}}^{\text{gr}}$ ) at 50 K obtained by measuring the voltage drop between contacts 5 and 4 ( $V_{54}$ ) while applying a current between contacts 7 and 1 ( $I_{71} = 1 \mu\text{A}$ ).  $R_{\text{sq}}^{\text{gr}}$  is determined using

$$R_{\text{sq}}^{\text{gr}} = (V_{54}/I_{71})(W_{\text{gr}}^{54}/L_{54}), \quad (\text{S2})$$

where  $W_{\text{gr}}^{54} = 0.80 \mu\text{m}$  is the average sample width between contacts 5 and 4 and  $L_{54} = 2.00 \mu\text{m}$  is the spacing between contacts 5 and 6 (Table I). From Fig. S3a, one can observe that  $R_{\text{sq}}$  shows a clear peak for  $V_{\text{bg}} = V_{\text{cnp}} = -5 \text{ V}$ , which corresponds to the CNP of this region.

Next, we study the  $V_{\text{bg}}$ -dependence of the  $R_{\text{sq}}$  of the  $\text{WSe}_2$ -covered graphene region ( $R_{\text{sq}}^{\text{gr/TMD}}$ ). For this purpose, we measure the voltage between contacts 4 and 3 ( $V_{43}$ ) while applying a DC current between contacts 7 and 1 ( $I_{71} = 1 \mu\text{A}$ ). We obtain  $R_{\text{sq}}$  using Equation S2 and changing  $V_{54}$  and  $L_{54}$  with  $V_{43}$  and  $L_{43} = 4.30 \mu\text{m}$ . Finally,  $W_{\text{gr}}^{43} = 0.85 \mu\text{m}$  is the average graphene flake width between contacts 3 and 4.  $R_{\text{sq}}^{\text{gr/TMD}}$  vs  $V_{\text{bg}}$  is shown in Fig. S3b and shows a peak at  $V_{\text{bg}} = V_{\text{cnp}} = -11 \text{ V}$  and an upturn at  $V_{\text{bg}} = -5 \text{ V}$ , which we attribute to the pristine graphene region between contacts 4 and 5. At 300 K, as shown in Figs. S3c and S3d, we obtain similar results with lower  $R_{\text{sq}}$  values near the CNP. We attribute this observation to the thermal energy broadening, which leads to an increased residual carrier density (and hence conductivity). From these measurements, we cannot rule out the opening of a small bandgap in BLG induced by a combination of the weak electric field applied by the  $V_{\text{bg}}$ [50, 51] and the field induced by the  $\text{WSe}_2$ [28, 29]. However, the similar  $R_{\text{sq}}$  at the charge neutrality point obtained at the  $\text{WSe}_2$ -covered and pristine BLG regions shows that the TMD is not opening a significant bandgap. Note that  $V_{\text{CNP}}$  also changes with temperature.

### Determination of the charge diffusivity

Because of the weak electron-electron interactions in graphene [52], in samples with moderate mobility, the charge ( $D_c$ ) and spin diffusivity ( $D_s$ ) have been shown to be equal [42]. Hence, it is useful to obtain  $D_c$  from the  $V_{\text{bg}}$  sweeps. For this purpose, we use the Einstein relation  $D_c = (e^2 R_{\text{sq}} \nu(E_F))^{-1}$ , where  $\nu(E_F)$  is the density of states at the Fermi level. Using the density of states of (ungapped) bilayer graphene, we obtain the following expression:

$$D_c = \frac{\pi \hbar^2 v_{f0}^2}{R_{\text{sq}} e^2 \sqrt{\gamma_1^2 + 4\pi \hbar^2 v_{f0}^2 |n|}}, \quad (\text{S3})$$

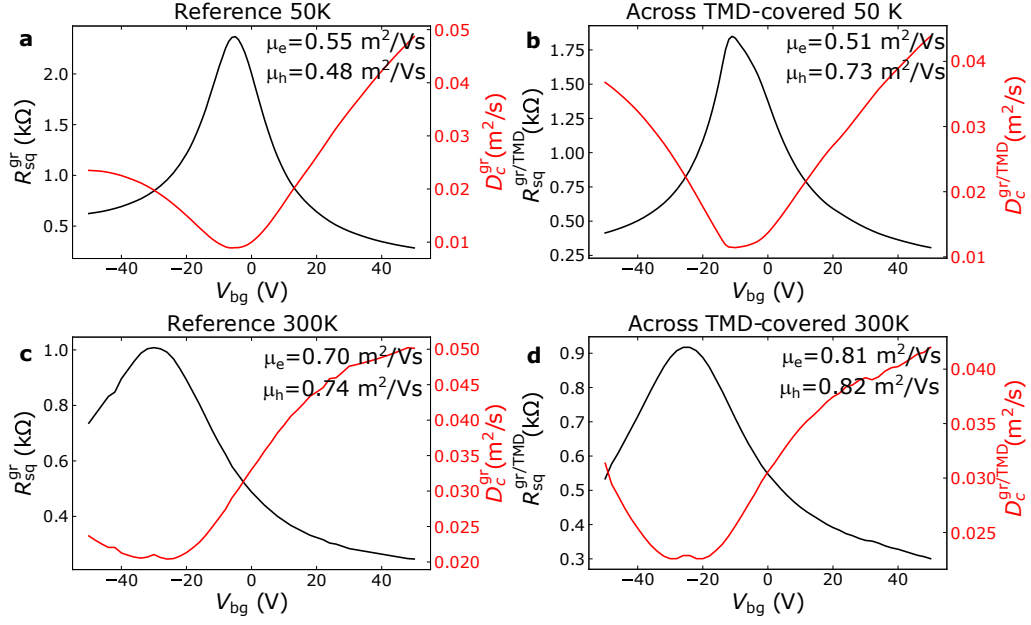


Figure S3. Charge transport characterization. (a) Square resistance  $R_{\text{sq}}^{\text{gr}}$  and charge diffusivity  $D_c^{\text{gr}}$  of the pristine BLG region as a function of  $V_{\text{bg}}$  at 50 K. (b)  $R_{\text{sq}}^{\text{gr/TMD}}$  and  $D_c^{\text{gr/TMD}}$  obtained across the WSe<sub>2</sub>-covered region vs  $V_{\text{bg}}$  at 50 K. (c)  $R_{\text{sq}}^{\text{gr}}$  and  $D_c^{\text{gr}}$  vs  $V_{\text{bg}}$  at 300 K. (d)  $R_{\text{sq}}^{\text{gr/TMD}}$  and  $D_c^{\text{gr/TMD}}$  vs  $V_{\text{bg}}$  at 300 K.

where  $v_{f0} = 1 \times 10^6$  m/s is the Fermi velocity of graphene,  $\gamma_1 \sim 0.4$  eV is the interlayer coupling parameter between pairs of orbitals on the dimmer sites in BLG [50], and  $\hbar$  is the reduced Planck constant. Using Equation S3, the measured  $R_{\text{sq}}$ , and  $n$  (obtained using Equation S1) we obtain  $D_c^{\text{gr}}$  for the pristine graphene region and  $D_c^{\text{gr/TMD}}$  for the WSe<sub>2</sub>-covered one. These results are shown as red lines in Figs. S3a-d. Note that, since we have performed the calculation assuming that the region between contacts 3 and 4 is all covered, our calculation is not very accurate near the CNP for Figs. S3b and S3d. Finally, to determine the charge transport quality of our device, we calculated the field-effect electron (hole) mobility ( $\mu_{e(h)}$ ) using  $R_{\text{sq}}^{-1} = ne\mu_{e(h)}$ , at  $V_{\text{bg}} - V_{\text{cnp}} = +(-)15$  V. The results are labeled in Fig. S3. We observe that the obtained mobilities are of about 5000 cm<sup>2</sup>/(Vs), as expected for graphene on SiO<sub>2</sub> devices. At 300 K, the mobilities are slightly higher than at 50 K, which we attribute to the broadening that leads to an underestimation of the carrier density close to the CNP. This is supported by the trend of  $D_c^{\text{gr}}$  and  $D_c^{\text{gr/TMD}}$ , that is higher at 300 K than at 50 K for all the  $V_{\text{bg}}$  range except for  $V_{\text{bg}} \gtrsim 40$  V, where  $D_c^{\text{gr}}$  and  $D_c^{\text{gr/TMD}}$  at 300 K start to saturate.

### Determination of the momentum scattering time and the Rashba SOC period

To confirm that the out-of-plane spins are in the weak spin-orbit coupling (SOC) regime, we determine the momentum scattering time ( $\tau_p$ ) from the charge transport measurements and compare it with the DFT values for the Rashba SOC precession frequency ( $\Omega_R$ ). To determine the momentum scattering time  $\tau_p$  in BLG, we use  $D_c = v_f^2 \tau_p / 2$ , where  $v_f$  is the Fermi velocity, that can be calculated using

$$v_f = \frac{1}{\hbar} \frac{dE(k)}{dk} = \frac{2\hbar v_{f0}^2 |k|}{\gamma_1} = \sqrt{2} v_{f0} \sqrt{\sqrt{1 + \frac{4|n|}{\alpha \gamma_1^2}} - 1}, \quad (\text{S4})$$

where  $k$  is the reciprocal lattice vector with respect to the K and K' points and  $\alpha = (\pi \hbar^2 v_{f0}^2)^{-1}$ . We replaced  $|k|$  by  $|n|$  using  $E = \hbar^2 v_{f0}^2 |k|^2 / \gamma_1$  and  $n = \int_0^{E_F} \nu(E) dE$ .

At 50 K and  $V_{\text{bg}} = -50$  V, since the CNP of the WSe<sub>2</sub>-covered BLG region is  $V_{\text{cnp}} = -11$  V, the carrier density  $n \approx 4.4 \times 10^{16}$  m<sup>-2</sup>. Hence,  $v_f \approx 1.06 \times 10^6$  m/s. Since  $D_c(V_{\text{bg}} = 50 \text{ V}) \approx 4.4 \times 10^{-2}$  m<sup>2</sup>/s,  $\tau_p = 2D_c/v_f^2 \approx 78$  fs.

From ab initio calculations,  $\lambda_R^{\text{grWSe}_2} = 0.56$  meV on monolayer graphene (Ref. 18). Since the calculation is performed at high carrier densities, we can safely assume no layer polarization is present [28, 29]. Hence, to obtain the average

Rashba SOC, we have to divide the monolayer graphene value by two  $\lambda_R^{\text{BLGWSe}_2} = \lambda_R^{\text{grWSe}_2}/2 = 0.28$  meV yielding a  $\Omega_R = 2\lambda_R^{\text{BLGWSe}_2}/\hbar = 0.85 \times 10^{12}$  rad/s and  $\tau_R = 2\pi/\Omega_R = 7.4$  ps. Hence,  $\tau_p/\tau_R \approx 1 \times 10^{-2}$ , which is much smaller than 1, confirming that the Rashba SOC is in the weak SOC regime.

Note that the proximity-induced spin-orbit parameters can depend on the rotation between the graphene and TMD layers [53, 54]. However, the maximum value of  $\lambda_R^{\text{WSe}_2}$  reported in Ref. 53 is  $\approx 0.88$  meV (note that  $\lambda_R^{\text{WSe}_2}$  has been normalized here by a factor of two to match the definitions with the other references followed here), leading to  $\tau_p/\tau_R^{\text{min}} \approx 3 \times 10^{-2}$ . We conclude that our results would apply for any rotation value if the interlayer distance corresponds to the DFT-calculated one.

### SPIN TRANSPORT AT THE PRISTINE GRAPHENE REGION AT 50 K

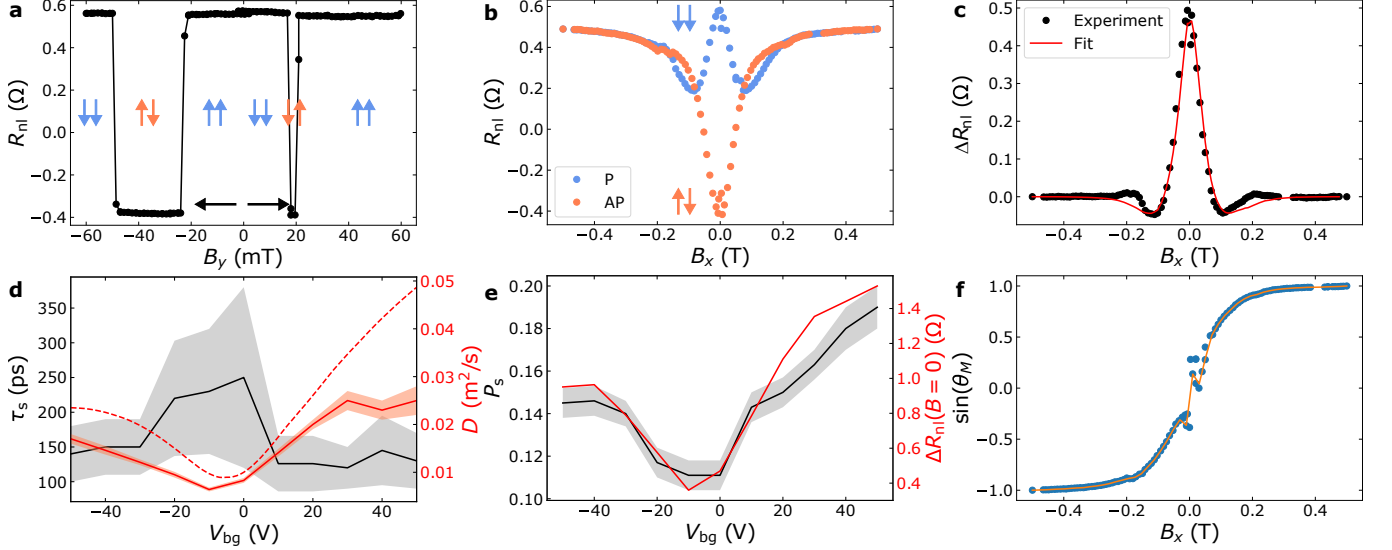


Figure S4. Spin transport at the pristine graphene region at 50 K. (a) Nonlocal spin valve measurement,  $R_{nl} = V_{57}/I_{41}$  as a function of  $B_y$ . (b) Nonlocal spin precession around  $B_x$  in the parallel (P) and antiparallel (AP) magnetic contact configurations ( $R_{nl}^P$  and  $R_{nl}^{AP}$ , respectively) at  $V_{bg} = 0$  V. (c)  $\Delta R_{nl} = (R_{nl}^P - R_{nl}^{AP})/2$  as a function of  $B_x$  obtained from the data in panel b (black solid circles) with its fit to the Bloch equations (red line). (d) Spin lifetime ( $\tau_s$ , black line), spin ( $D_s$ , red solid line) and charge ( $D_c$ , red dashed line) diffusivity. (e) Contact spin polarization ( $P_s = \sqrt{P_i P_d}$ ) together with  $\Delta R_{nl}(B = 0)$ . (f)  $\sin(\theta_M)$  obtained from the data in panel b (blue solid circles). The orange line is a guide to the eye.

We performed measurements in the nonlocal configuration in the pristine graphene region to determine the spin transport properties of our system at 50 K. In particular, we applied a current between contacts 4 and 1 ( $I_{41}$ ) and measure the nonlocal voltage between contacts 5 and 7 ( $V_{57}$ ). The spin valve and spin precession measurements are shown in Figs. S4a and S4b, respectively. From Fig. S4a, we observe that the spin signal is around  $0.5 \Omega$  and contacts 4 and 5 switch at very similar  $B_y$  values for positive  $B_y$ , giving rise to a very narrow antiparallel state. Note that, in contrast with the spin transport measurements performed across the WSe<sub>2</sub>-covered BLG region (see Fig. 2b of the main manuscript),  $R_{nl}$  is higher for the parallel (P) than the antiparallel (AP) state, as expected for standard nonlocal measurements. The next step is to apply  $B_x$  to induce spin precession. We performed this experiment by taking the sweeps for negative and positive  $B_x$  to control the magnetization state separately. Figure S4b shows the nonlocal resistance in the P ( $R_{nl}^P$ ) and AP ( $R_{nl}^{AP}$ ) magnetization configurations as indicated by the arrows. At low  $B_x$ , the spins injected along  $y$  precess around the magnetic field leading to the crossing between the P and AP curves at  $B_x \approx \pm 65$  mT. As  $B_x$  increases, the contact magnetizations get pulled towards  $x$ . The spins that are now polarized along  $x$  do not precess, giving rise to the saturation of both  $R_{nl}^P$  and  $R_{nl}^{AP}$  at the value of  $R_{nl} = R_{nl}^P(B_x = 0)$ . Taking the contact pulling into account, the measured signal is

$$R_{nl}^{P(AP)} = \pm \cos^2(\theta_M) f_{prec} + \sin^2(\theta_M) f_{prec}(B = 0). \quad (S5)$$

Here,  $f_{prec}$  is the spin precession signal,  $\theta_M$  is the contact magnetization angle with respect to the easy axis.

We first isolate the spin precession signal by plotting  $\Delta R_{\text{nl}} = (R_{\text{nl}}^{\text{P}} - R_{\text{nl}}^{\text{AP}})/2$  in Fig. S4c. To obtain the spin transport parameters of this region, we fit the spin precession data to  $\Delta R_{\text{nl}} = \cos^2(\theta_M) f_{\text{prec}}$ . Here we use the solution of the Bloch equations for a homogeneous system taking into account the spin backflow in the spin injector and detector contacts 4 and 5 as  $f_{\text{prec}}(P, \tau_s^{\text{gr}}, D_s^{\text{gr}}, R_{\text{ci}}, R_{\text{cd}}, L_{54}, W_s^{54})$ , which is a function of  $P = \sqrt{P_i P_d}$ , where  $P_{i(d)}$  is the spin injection (detection) efficiency,  $\tau_s^{\text{gr}}$  the spin lifetime,  $D_s^{\text{gr}}$  the diffusivity of the pristine graphene region,  $R_{\text{ci}(d)}$  the contact resistance of the spin injector (detector) (Refs. 55 and 56).  $\lambda_s^{\text{gr}} = \sqrt{\tau_s^{\text{gr}} D_s^{\text{gr}}}$  is the spin relaxation length.

To perform the fit, one needs to know  $\theta_M$ . We obtain it by using Equation S6:

$$\sin(\theta_M) = \text{sgn}(B_x) \sqrt{\frac{R_{\text{nl}}^{\text{avg}} - \min(R_{\text{nl}}^{\text{avg}})}{\max(R_{\text{nl}}^{\text{avg}}) - \min(R_{\text{nl}}^{\text{avg}})}} \quad (\text{S6})$$

where  $R_{\text{nl}}^{\text{avg}} = (R_{\text{nl}}^{\text{P}} + R_{\text{nl}}^{\text{AP}})/2$ ,  $\text{sgn}(B_x)$  is the sign of the magnetic field, and  $\max(R_{\text{nl}}^{\text{avg}})$  and  $\min(R_{\text{nl}}^{\text{avg}})$  are the maximum and minimum values of  $R_{\text{nl}}^{\text{avg}}$ , respectively. The result of this operation is shown in Fig. S4f and is used to fit the data, shown as the red line of Fig. S4c. We have performed this operation for  $V_{\text{bg}} = -50$  to 50 V. In Fig. S4d, we plot the extracted  $\tau_s^{\text{gr}}$  (black line) with its error range (grey area) and  $D_s^{\text{gr}}$  (red line) and its error range (light orange area). The dashed line corresponds to  $D_c^{\text{gr}}$  (Fig. S3a), which is in reasonable agreement with  $D_s^{\text{gr}}$  as expected. The apparent saturation of  $D_s^{\text{gr}}$  at positive  $V_{\text{bg}}$  is likely caused by the contact pulling, that determines the data at high  $B_x$ . We also note that  $D_s^{\text{gr}}$  and  $\tau_s^{\text{gr}}$  show opposite trend with  $V_{\text{bg}}$ . Hence,  $\lambda_s^{\text{gr}}$  shows little change with  $V_{\text{bg}}$ . As a consequence, the contact spin polarization ( $P_s = \sqrt{P_i P_d}$ ) shown in Fig. S4e follows closely the spin signal magnitude ( $\Delta R_{\text{nl}}(B = 0)$ ). Finally, we note that the spin signal is positive for all the  $V_{\text{bg}}$  values, ranging from 0.4 up to 1.5  $\Omega$ . This result is also consistent with the WSe<sub>2</sub>-covered region being responsible for the sign reversal.

### SPIN TRANSPORT ACROSS THE WSe<sub>2</sub>-COVERED GRAPHENE REGION AT 50 K

To study spin transport in the WSe<sub>2</sub>-covered region at 50 K, we measured the nonlocal resistance by applying a current  $I_{\delta 1}$  between contacts 3 and 1 and measuring the voltage  $V_{\delta 1}$  between contacts 4 and 7. The nonlocal spin valve measurements are performed by taking  $R_{\text{nl}} = V_{\delta 1}/I_{\delta 1}$  as a function of the magnetic field applied along the  $y$  direction ( $B_y$ ). As we sweep  $B_y$ , the contact magnetizations are controlled independently due to the different coercivities of the contacts. In Fig. S5a, we can observe two abrupt changes of  $R_{\text{nl}}$  for positive and negative  $B_y$ , which correspond to switches of the magnetization of contacts 4 and 3. The  $R_{\text{nl}}^{\text{AP}}$  is higher than  $R_{\text{nl}}^{\text{P}}$ . In Figs. S5a, c, e, g, and i, we show the nonlocal spin valve measurements performed at  $V_{\text{bg}} = -60, -50, -30, 40,$  and 50 V, respectively, where one can see that  $R_{\text{nl}}^{\text{AP}}$  is higher than  $R_{\text{nl}}^{\text{P}}$  for all the backgate voltages, as in the main manuscript. The only exception is at  $V_{\text{bg}} = -30$  V, where  $\Delta R_{\text{nl}}$  is smaller than the noise level ( $\sim 0.5$  m $\Omega$ ). We also performed nonlocal spin precession measurements applying  $B_x$  for the five  $V_{\text{bg}}$  values mentioned, as shown in Figs. S5b, d, f, h, and j. The insets show the low  $B_x$  region, which confirm that  $R_{\text{nl}}^{\text{P}}$  and  $R_{\text{nl}}^{\text{AP}}$  do not cross, with the exception of  $V_{\text{bg}} = -30$  V, where the in-plane signal is smaller than the noise level and both curves touch. This confirms the robustness of our measurements with  $V_{\text{bg}}$ .

### SPIN DRIFT EXPERIMENTS ACROSS THE WSe<sub>2</sub>-COVERED REGION AT 50 K

We perform spin drift experiments across the WSe<sub>2</sub>-covered BLG region using the circuit shown in Fig. S6a, with the delta current ( $I_{\delta 2}$ ) applied between contacts 3 and 1, the delta voltage ( $V_{\delta 2}$ ) measured between contacts 5 and 7, and the DC current ( $I_{\text{DC}}$ ) applied between contacts 4 and 1 to induce drift.

To determine the evolution of  $\Delta R_{\text{nl}}$  with  $I_{\text{DC}}$  and  $V_{\text{bg}}$ , we performed nonlocal spin valve measurements in the configuration of Fig. S6a. The results from these measurements are shown in Fig. S6. Figure S6b shows the results presented in Fig. 3c of the main manuscript and the data for  $V_{\text{bg}} = -40$  V. The corresponding spin valve measurements are shown in Figs. S6d, S6e, and S6f and one can clearly see the crossing between  $R_{\text{nl}}^{\text{P}}$  and  $R_{\text{nl}}^{\text{AP}}$  at  $I_{\text{DC}} = 0$  in both cases. The results obtained at  $V_{\text{bg}} = -8$  V are shown in Figs. S6c and S6g and, in contrast with the other measured  $V_{\text{bg}}$  values,  $\Delta R_{\text{nl}}$  remains positive in the whole  $I_{\text{DC}}$  range. The increase in  $\Delta R_{\text{nl}}$  for positive and negative  $I_{\text{DC}}$  is attributed to the opposite doping of the WSe<sub>2</sub>-covered and pristine BLG regions which have comparable lengths. Figures S6f and S6g show the data at  $V_{\text{bg}} = 40$  V, which yields a similar trend as for  $V_{\text{bg}} = -50$  V. Negative  $\Delta R_{\text{nl}}$  has also been observed for  $I_{\text{DC}} = 60$   $\mu\text{A}$  at  $V_{\text{bg}} = 5, 10,$  and 20 V (not shown). As can be seen from the data, in some cases, there are large spikes in  $R_{\text{nl}}$  when the magnetization switches. Since we do not know the origin of these one-point artifacts, we filter them out to quantify  $\Delta R_{\text{nl}}$ .

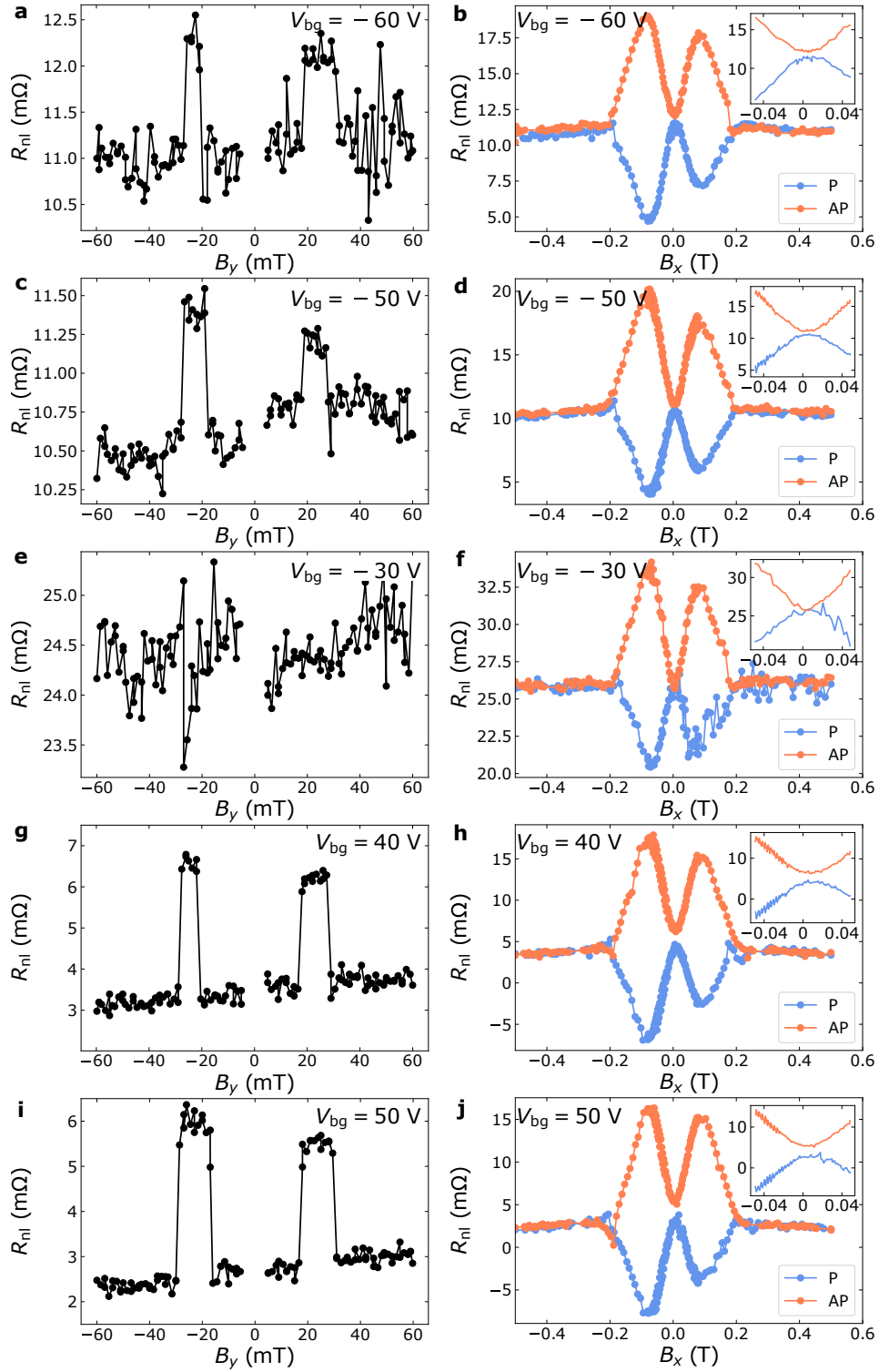


Figure S5. Spin transport across the WSe<sub>2</sub>-covered BLG region at 50 K. (a), (c), (e), (g) and (i) Nonlocal spin valve measurements and (b), (d), (f), (h) and (j) nonlocal spin precession measurements performed at  $V_{bg} = -60, -50, -30, 40, \text{ and } 50$  V. The insets are a zoom of the low  $B_x$  range.

The evolution of the nonlocal spin precession data with  $I_{DC}$  at  $V_{bg} = -50$  and  $-30$  V is shown in Fig S7. The top panels (Figs. S7a-d) correspond to  $V_{bg} = -50$  V and the bottom ones (Figs. S7e-h) correspond to the  $V_{bg} = -30$  V case. In the latter, because  $R_{nl}^P < R_{nl}^{AP}$  at  $B_x = 0$ , the in-plane spin signal  $[\Delta R_{nl}(B_x = 0)] = (R_{nl}^P(B_x = 0) -$

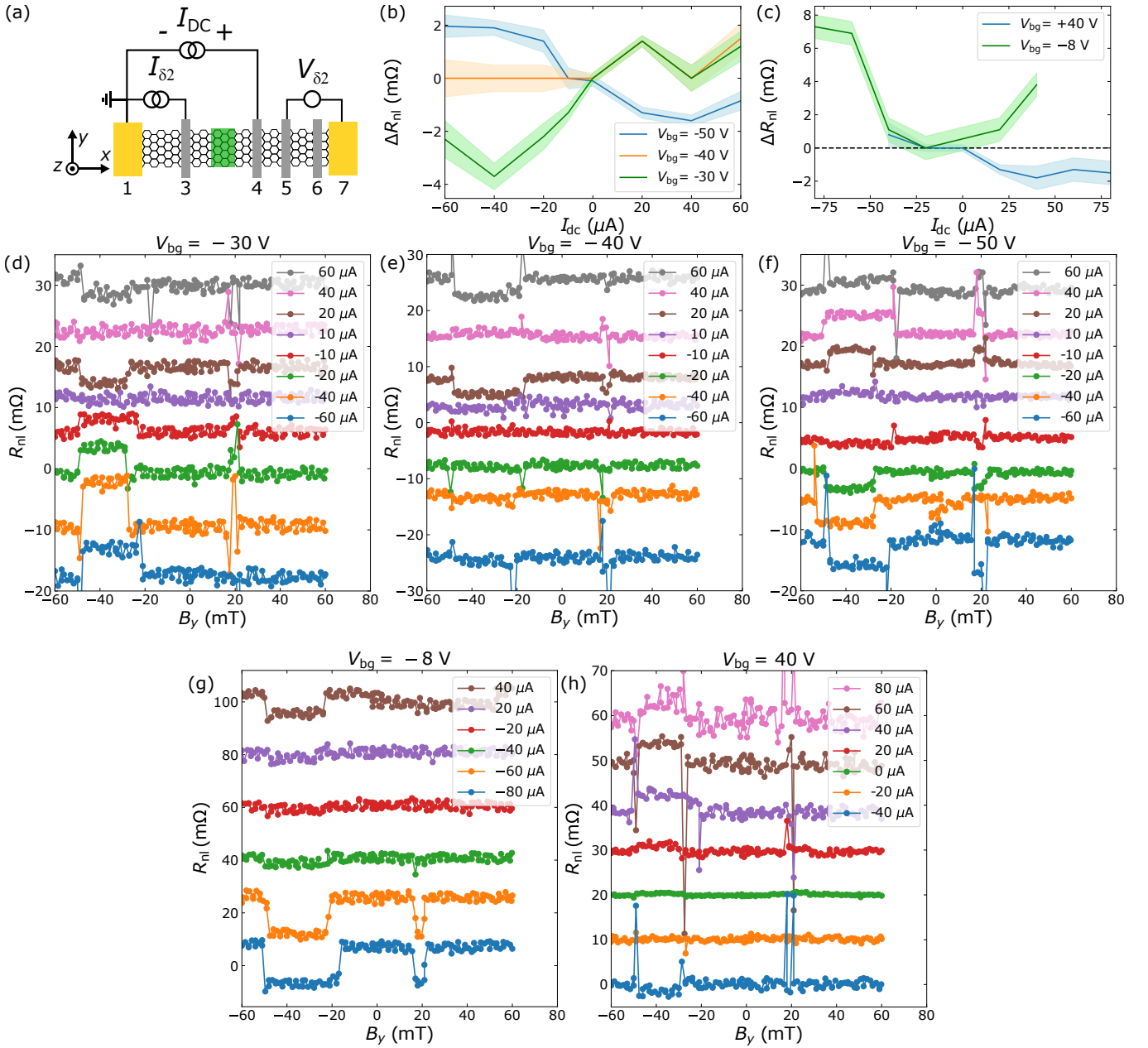


Figure S6. Nonlocal spin valve measurements as a function of  $I_{DC}$  and  $V_{bg}$  at 50 K. (a) Sketch of the measurement configuration. (b)  $\Delta R_{nl}$  vs  $I_{DC}$  at  $V_{bg} = -50, -40$  and  $-30$  V taken from data in panels b and c. (c)  $\Delta R_{nl}$  vs  $I_{DC}$  at  $V_{bg} = -8$  and  $40$  V taken from the data in panels g and h. (d), (e), (f), (g) and (h) Nonlocal spin valve measurements as a function of  $I_{DC}$  for  $V_{bg} = -50, -40, -30, -8,$  and  $40$  V, respectively.

$R_{nl}^{AP}(B_x = 0)/2]$  decreases with  $I_{DC}$  while their absolute value increases. We also observe that the out-of-plane signal [ $\Delta R_{nl}(B_x \sim \pm 100)$  mT] increases with the applied  $I_{DC}$ , as expected for standard spin drift experiments. In contrast, for  $V_{bg} = -50$  V,  $\Delta R_{nl}(B_x = 0)$  increases as  $I_{DC}$  decreases while the out-of-plane spin signal changes weakly from 1.5 to 2 m $\Omega$ . As a result, for  $I_{DC} = -40$   $\mu$ A (Fig. S7d), the in-plane spin signal is significantly larger than the out-of-plane one, as in conventional spin precession measurements in isotropic systems.

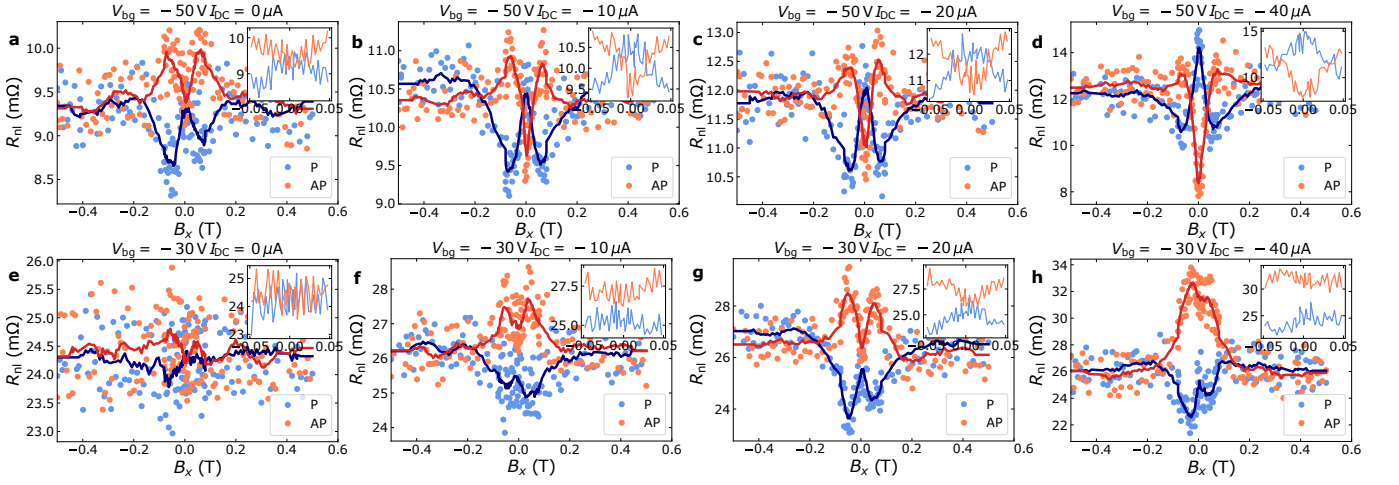


Figure S7. Nonlocal spin precession measurements as a function of  $V_{bg}$  and  $I_{DC}$  at 50 K. (a-d) Spin precession measurements at  $V_{bg} = -50$  and different  $I_{DC}$  values (0 to  $-40 \mu\text{A}$ ). (e-h) Spin precession measurements at  $V_{bg} = -30$  and different  $I_{DC}$  values (0 to  $-40 \mu\text{A}$ ). The insets correspond to the low  $B_x$  range and the solid lines have been obtained averaging a window of eleven points.

### SPIN DRIFT EXPERIMENTS ACROSS THE $WSE_2$ -COVERED REGION AT 300 K

In this section, to complement the room temperature results presented in the main manuscript, we show the results from the spin drift experiments performed at 300 K. In Fig. S8, we plot the nonlocal spin valve measurements used to obtain  $\Delta R_{nl}$  in Fig. 4 of the main manuscript. In this case, we observe that, at fixed  $I_{DC}$ ,  $\Delta R_{nl}$  changes sign once, at  $V_{bg} \approx -30$  V and decreases at  $V_{bg} = 50$  V, indicating that there might be another sign change for  $V_{bg} > 50$  V. Furthermore,  $\Delta R_{nl}$  is reversed by changing the sign of  $I_{DC}$ , as at 50 K. We also measured the spin precession data at  $V_{bg} = -50$  and  $+25$  V and  $I_{DC} = \pm 40 \mu\text{A}$ . The results are shown in Fig. S9 and show that, while the in-plane spin signal reverses sign, the out-of-plane spin signal remains positive in all the cases. Note that, despite the significantly smaller signal in Fig. S9b,  $R_{nl}^P$  clearly crosses  $R_{nl}^{AP}$  at  $B_x \approx \pm 80$  mT.

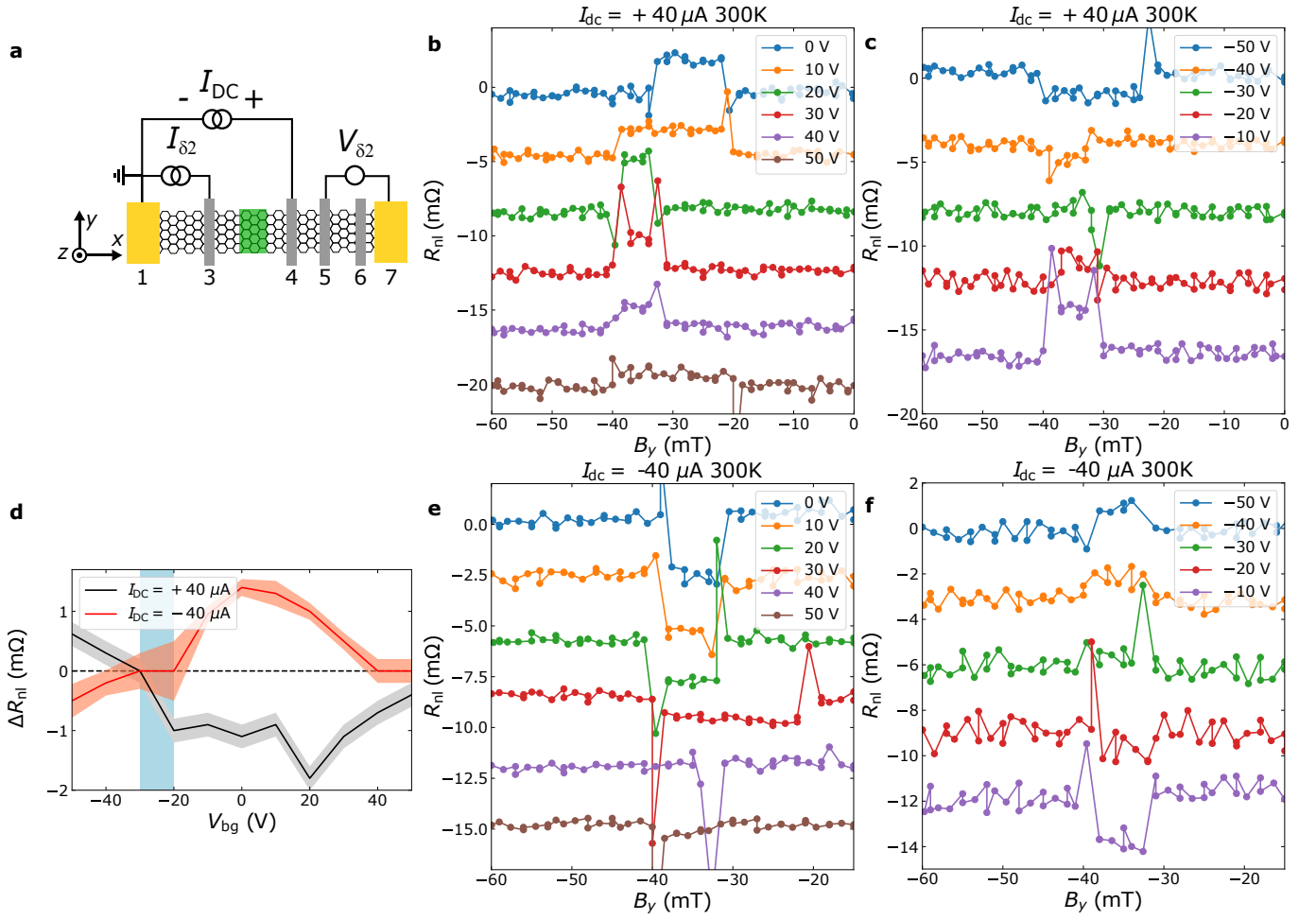


Figure S8. Room temperature nonlocal spin valve measurements as a function of  $V_{bg}$  for  $I_{DC} = \pm 40 \mu A$ . (a) Sketch of the measurement configuration. (b), (c) Spin valve measurements obtained at  $I_{DC} = +40 \mu A$  for different  $V_{bg}$  values. The curves are offset for clarity. (e), (f) Nonlocal spin valve measurements obtained at  $I_{DC} = -40 \mu A$  for different  $V_{bg}$  values. The curves are offset for clarity. (d)  $\Delta R_{nl}$  vs  $V_{bg}$  for  $I_{DC} = \pm 40 \mu A$ , as shown in Fig. 4 of the main manuscript, taken from the data in panels b, c, e, and f.

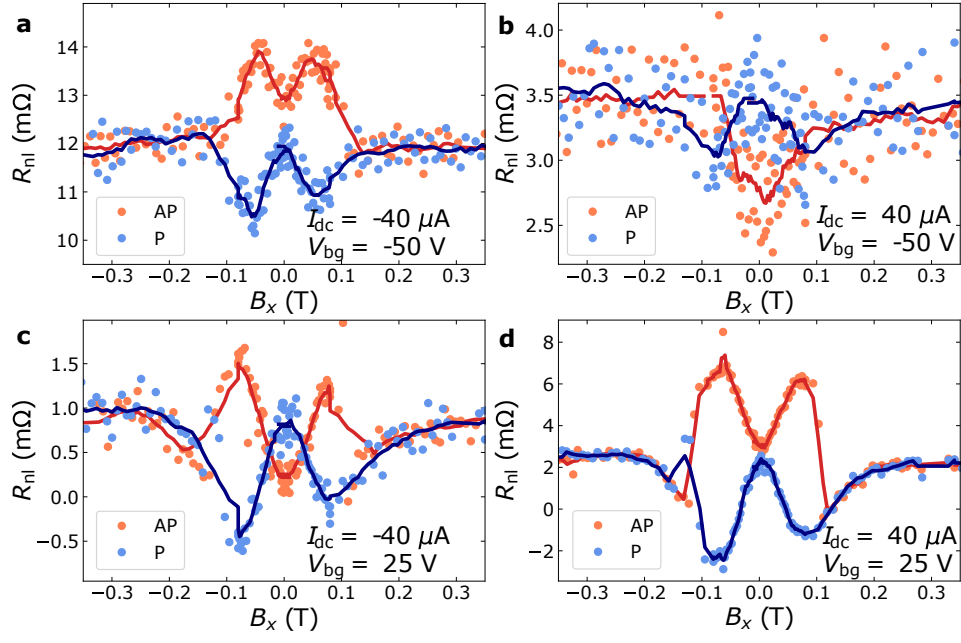


Figure S9. Room temperature nonlocal spin precession measurements at different  $V_{bg}$  and  $I_{DC}$  values.  $R_{nl}$  vs  $B_x$  for  $V_{bg} = -50$  V and  $I_{DC} = -40$   $\mu$ A (a) and  $I_{DC} = +40$   $\mu$ A (b);  $V_{bg} = +25$  V and  $I_{DC} = -40$   $\mu$ A (c) and  $I_{DC} = +40$   $\mu$ A (d).

## SPIN DRIFT EXPERIMENTS AT THE PRISTINE GRAPHENE REGION AT 300 K

To confirm that the anomalous  $I_{\text{DC}}$ -dependence reported here is caused by the  $\text{WSe}_2$ -covered region, we performed spin drift experiments in the pristine BLG region. The measurement configuration is shown in Fig. S10a. The spins are injected by applying a delta current  $I_{\delta 3}$  between contacts 4 and 2. Note that, even though contact 2 may inject some spins, most of them relax in the  $\text{WSe}_2$ -covered BLG region and no additional switches were observed in the nonlocal spin valve measurements. The nonlocal signal ( $V_{\delta 3}$ ) is measured between contacts 6 and 7, that is a non-magnetic electrode. Finally,  $I_{\text{DC}}$  is applied between contacts 5 and 2 to induce drift. In Fig. S10b, we show the evolution of  $\Delta R_{\text{nl}}$  with  $I_{\text{DC}}$  for different values of  $V_{\text{bg}}$ . We observe that, for  $V_{\text{bg}} = -50$  and  $-30$  V,  $\Delta R_{\text{nl}}$  decreases as  $I_{\text{DC}}$  increases. Looking at Fig. S3c, one realizes that the CNP of the pristine BLG region at 300 K occurs at  $V_{\text{bg}} \approx -27$  V, thus, the channel is hole doped for  $V_{\text{bg}} = -50$  and  $-30$  V. In this case, the application of a positive  $I_{\text{DC}}$  makes holes drift from contact 5 to contact 2, opposing spin transport. Hence,  $\Delta R_{\text{nl}}$  is expected to decrease as  $I_{\text{DC}}$  increases. In contrast, for  $V_{\text{bg}} = -10, 10, 30,$  and  $50$  V,  $\Delta R_{\text{nl}}$  increases with  $I_{\text{DC}}$ . This observation is consistent with the fact that electrons in the channel propagate in the opposite direction of  $I_{\text{DC}}$ , flowing from contact 2 to 5 for  $I_{\text{DC}} > 0$ , and giving rise to an enhancement of  $\Delta R_{\text{nl}}$  with  $I_{\text{DC}}$  [46, 47]. These results imply that the anomalous  $I_{\text{DC}}$ -dependence of  $\Delta R_{\text{nl}}$  measured across the  $\text{WSe}_2$ -covered BLG channel is induced by the unconventional spin transport in the latter.

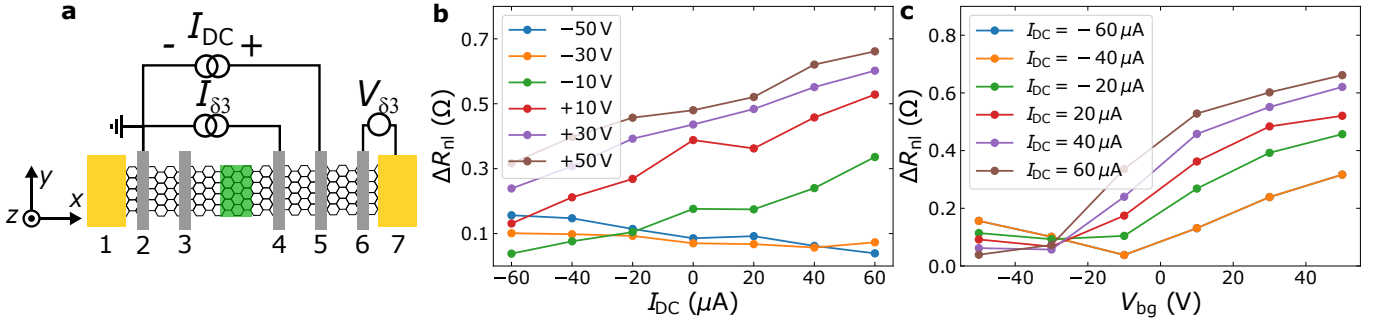


Figure S10. Room temperature spin drift experiments in the pristine BLG region. (a) Sketch of the measurement configuration. (b)  $I_{\text{DC}}$ -dependence of  $\Delta R_{\text{nl}}$  at different  $V_{\text{bg}}$  values. (c)  $V_{\text{bg}}$ -dependence of  $\Delta R_{\text{nl}}$  at different  $I_{\text{DC}}$  values.

## REPRODUCIBILITY

In addition to the device reported until this point (device 1), we prepared another sample (device 2) using the same recipe (reported in the Methods section of the main manuscript) and obtained very similar results, showing the robustness of our findings in BLG/ $\text{WSe}_2$  van der Waals heterostructures. The optical microscope image of the device and the  $V_{\text{bg}}$ -dependence of  $\Delta R_{\text{nl}}$  for two different  $I_{\text{DC}}$  values are shown in Fig. S11.

As in Fig. 2d and 3b of the main manuscript, the sign of  $\Delta R_{\text{nl}}$  in the non-local spin valve configuration reverses close to the CNP of the BLG region proximitized with  $\text{WSe}_2$ . Sweeping  $V_{\text{bg}}$  controls the amplitude and the sign of the spin signal, as shown in Fig. S11b. Due to the width of the  $\text{WSe}_2$ -covered graphene region being  $1.4 \mu\text{m}$  (narrower than in device 1), the amplitude of the spin signal is roughly ten times larger than in device 1, and the signal-to-noise ratio of  $\Delta R_{\text{nl}}$  is higher. As shown in the inset of Fig. 1b of the main manuscript, when the width of the  $\text{WSe}_2$  flake is designed so that the position where  $\mu_{\text{sy}}$  changes sign ( $x_0$ ) lies within the proximitized region, the sign of  $\Delta R_{\text{nl}}$  can be controlled by the applied  $I_{\text{DC}}$ . Indeed, for the full range of  $V_{\text{bg}}$  values, reversing the sign of  $I_{\text{DC}}$  reverses the sign of the spin signal. This shows that we have achieved the electrical control of spin reversal in two independent ways without the need for a magnetic field in two different BLG/TMD heterostructures.

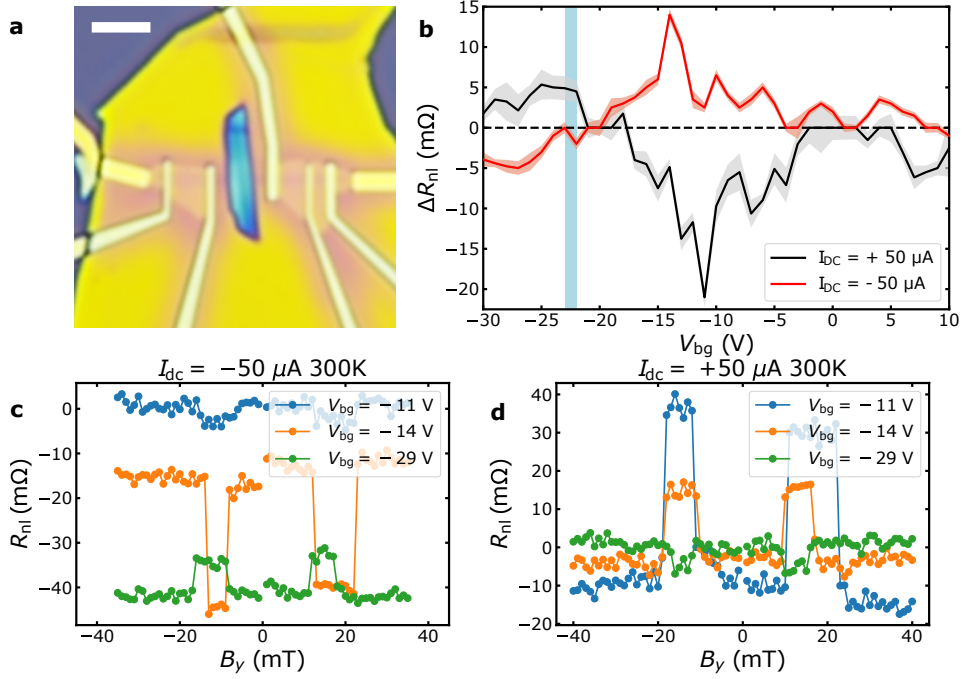


Figure S11. Spin drift experiments in device 2 at 100 K. (a) Optical image of device 2. The vertical WSe<sub>2</sub> flake (blue) and Co electrodes (light grey) are visible below the hBN flake (yellow) used to cap the device. The horizontal graphene flake is barely visible as a darker strip underneath the electrodes and the TMD flake. The scale bar is 3  $\mu\text{m}$ . For the spin drift measurements, the same configuration as in Fig. S8a was used. (b)  $V_{\text{bg}}$ -dependence of  $\Delta R_{\text{nl}}$  for  $I_{\text{DC}} = \pm 50 \mu\text{A}$  and  $I_{\delta 2} = 50 \mu\text{A}$ . The blue vertical strip represents the CNP of the WSe<sub>2</sub>-covered region. The light grey and red areas represent the experimental error range calculated using the standard deviation associated with the statistical average of  $R_{\text{nl}}^{\text{P}}$  and  $R_{\text{nl}}^{\text{AP}}$ . (c) and (d) Nonlocal spin valve measurements at  $I_{\text{DC}} = -/+ 50 \mu\text{A}$ , respectively and at  $V_{\text{bg}} = -11, -14, \text{ and } -29 \text{ V}$ .

### INFLUENCE OF THE ANNEALING TEMPERATURE AND WSe<sub>2</sub> WIDTH ON THE PROXIMITY-INDUCED SOC

The data of four additional devices are shown here to illustrate the influence of the annealing temperature, and thus SOC strength, on the spin transport. Devices 3 to 6, shown in Figs. S12a-d, are fabricated following the recipe of device 1 and 2 (see the Methods section of the main manuscript) with small variations. None of the samples were capped with Au and hBN, which does not influence the measurements but makes the Co electrodes more prone to oxidation during transfer to the cryostat. The strength of the proximity-induced SOC directly depends on the interface between graphene and the TMD flake. Some van der Waals heterostructures have a self-cleaning mechanism. Hence, after annealing, the contamination between the layers clusters in pockets and the remaining contact areas are cleaned [57]. Accordingly, device 3, which was not annealed, shows a conventional positive nonlocal spin valve signal with a large amplitude (Fig. S12e) as for pristine graphene samples. Also, the spin precession data (Fig. S12i) has a similar shape as for isotropic systems, since a small proximity-induced SOC also leads to a negligible anisotropy in the spin transport. Along these lines, device 4, which was annealed for 1 h as all other devices, but at a lower temperature (400  $^{\circ}\text{C}$ ), shows anisotropic spin precession (Fig. S12j) but no negative sign of  $\Delta R_{\text{nl}}$  (Fig. S12f). Here, the annealing led to a significant proximity-induced SOC but, due to the lower annealing temperature, it did not reach the strong SOC regime. We suspect that the dominating factor for the resulting strength of the induced SOC after the annealing is the temperature of the process and that the duration and the pressure only play a secondary role. This seems to agree with findings in the fabrication of other graphene/TMD heterostructures [25]. The fabrication of devices 5 and 6 included an additional electron beam lithography and reactive ion etching step to structure the graphene flake into a double H-bar shape before fabricating the Au contacts and Co electrodes. This enables us to also measure the spin-to-charge conversion by spin Hall effect in graphene due to the proximity-induced SOC as reported in Ref. 58. Both samples were annealed at 430  $^{\circ}\text{C}$  for 1 h but have different widths of the WSe<sub>2</sub> flake, 790 and 250 nm, respectively, as obtained from scanning electron microscopy images. The wider flake leads to a longer transport in proximitized graphene, reaching the region where  $\Delta R_{\text{nl}}$  has a negative sign (in Fig. 1b of the main manuscript, we estimate this region for a width between 750 and 1750 nm for  $\tau_{\text{IV}} = 156 \text{ fs}$ ). Accordingly, the diffusive spin transport data from

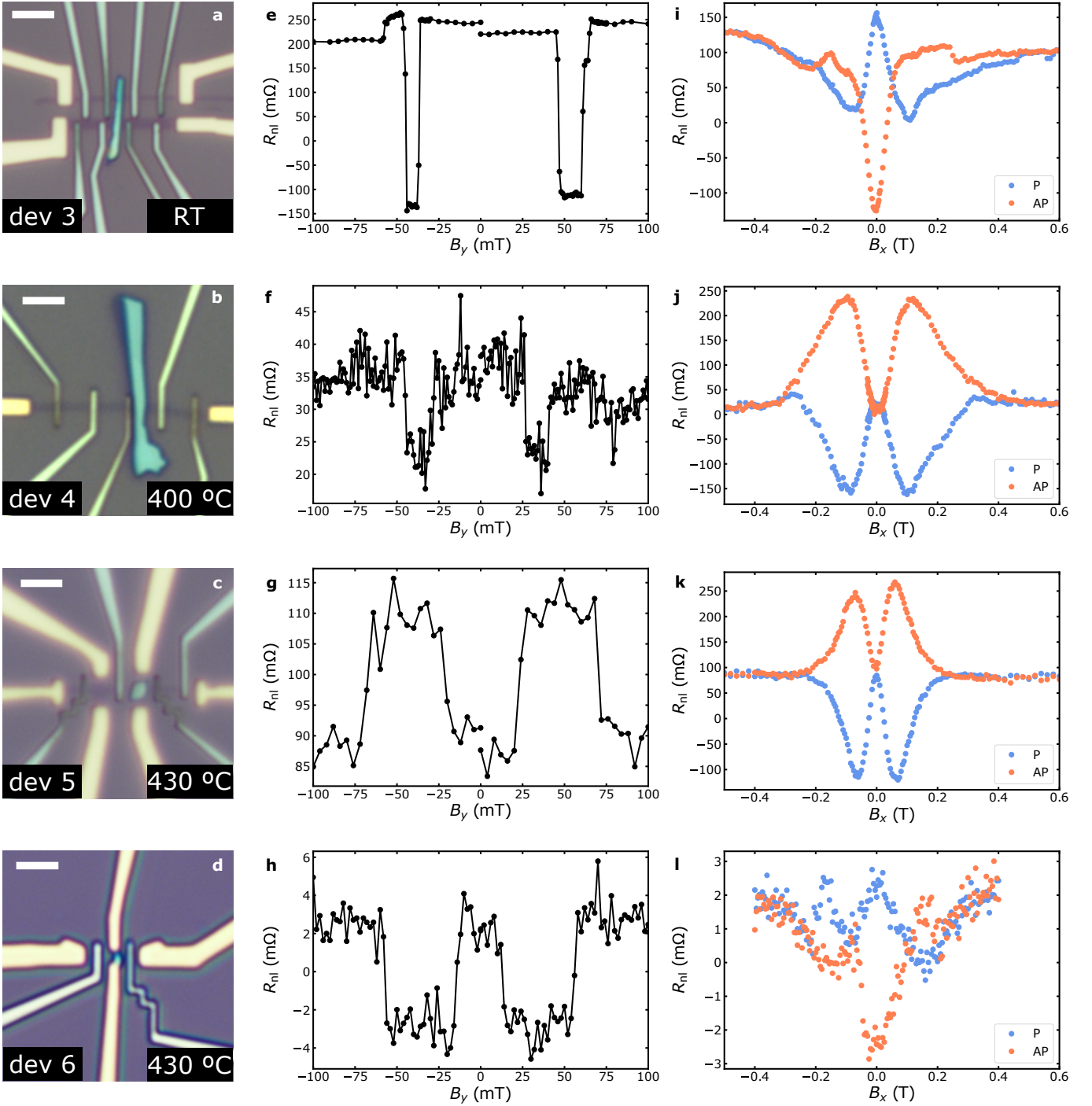


Figure S12. The influence of SOC strength on the spin transport. (a)-(d) Optical image of additional measured devices. The scale bar is  $3 \mu\text{m}$ . (e)-(h) Nonlocal spin valve measurement across the  $\text{WSe}_2$ -covered graphene region as a function of the magnetic field applied along  $y$  ( $B_y$ ). (i)-(l) Nonlocal spin precession measurements with the magnetic field applied along  $x$  ( $B_x$ ) for the parallel (P) and antiparallel (AP) configurations. The measurement temperatures are 10 K for (e) and (i); 100 K for (f), (g), (j) and (k) and 300 K for (h) and (l).

device 5 (Figs. S12g and k) is analogous to the one shown in Figs. 2b and d. For the narrower device 6, the measured data resembles the typical behavior for spin precession in isotropic media. This is caused by the fact that the  $\text{WSe}_2$  width is smaller than the in-plane spin lifetime [59], reducing the total in-plane spin relaxation.

TABLE II. Modelling parameters.

$\lambda_{\text{VZ}}$ (meV)	$\Omega_{\text{VZ}}$ (s <sup>-1</sup> )	$D_s$ (m <sup>2</sup> /s)	$\tau_s^\perp$ (ps)	$W_{\text{TMD}}$ ( $\mu\text{m}$ )	$W_{\text{gr}}$ ( $\mu\text{m}$ )
0.595	$1.808 \times 10^{12}$	0.02	30	5	0.5

### MODELING DETAILS

The plot shown in Fig. 1b, that confirms that our explanation is consistent with the current understanding of BLG/TMD heterostructures, is realized using spin transport calculations. In particular, assuming  $\tau_p \Omega_{\text{R}} \ll 1$  (weak SOC regime for  $\tau_s^\perp$ ), we use the drift-diffusion equations for each valley separately [60]:

$$\frac{d\vec{\mu}_s^{\text{K}}}{dt} = D_s \frac{d^2 \vec{\mu}_s^{\text{K}}}{dx^2} - v_d \frac{d\vec{\mu}_s^{\text{K}}}{dx} - \frac{\vec{\mu}_s^{\text{K}}}{\tau_s^\perp} + \vec{\Omega}_{\text{VZ}} \times \vec{\mu}_s^{\text{K}} - \frac{\vec{\mu}_s^{\text{K}} - \vec{\mu}_s^{\text{K}'}}{2\tau_{\text{iv}}} \quad (\text{S7})$$

$$\frac{d\vec{\mu}_s^{\text{K}'}}{dt} = D_s \frac{d^2 \vec{\mu}_s^{\text{K}'}}{dx^2} - v_d \frac{d\vec{\mu}_s^{\text{K}'}}{dx} - \frac{\vec{\mu}_s^{\text{K}'}}{\tau_s^\perp} - \vec{\Omega}_{\text{VZ}} \times \vec{\mu}_s^{\text{K}'} - \frac{\vec{\mu}_s^{\text{K}'} - \vec{\mu}_s^{\text{K}}}{2\tau_{\text{iv}}} \quad (\text{S8})$$

where,  $\vec{\mu}_s^{\text{K(K}' )} = (\mu_{sx}^{\text{K(K}' )}, \mu_{sy}^{\text{K(K}' )}, \mu_{sz}^{\text{K(K}' )})$  is the  $x, y, z$ -polarized spin accumulation in valley K(K'). The first term at the right hand side accounts for spin diffusion with a diffusivity  $D_s$  and the second term introduces spin relaxation with a rate

$$(\overline{\tau_s^\perp})^{-1} = \begin{pmatrix} (2\tau_s^\perp)^{-1} & 0 & 0 \\ 0 & (2\tau_s^\perp)^{-1} & 0 \\ 0 & 0 & (\tau_s^\perp)^{-1} \end{pmatrix}, \quad (\text{S9})$$

that induces an anisotropy of 1/2. The third term induces spin precession around the VZ-SOF  $\vec{\Omega}_{\text{VZ}} = (0, 0, \Omega_{\text{VZ}})$  and the last one accounts for intervalley scattering at a rate  $\tau_{\text{iv}}^{-1}$ . Note that VZ-SOF fluctuations may lead to extra in-plane spin relaxation [7] which is not included in the model but should not lead to net spin precession.

### Weak SOC regime

To confirm that the output of our model agrees with the existing theory in the weak SOC regime ( $\tau_{\text{iv}} \ll \tau_{\text{VZ}}$ ), we have solved Eqs. S7 and S8 in the steady state ( $d\vec{\mu}_s^{\text{K(K}' )}/dt = 0$ ) using the parameters displayed in Table II. This operation is performed numerically as a boundary value problem using Python's Scipy package. We solve the problem in the range  $0 < x < 5 \mu\text{m}$  and, to set the boundary conditions, we define the spin current as follows:

$$\vec{I}_s^{\text{K(K}' )} = \frac{W_{\text{gr}}}{eR_{\text{sq}}} \left( -\frac{d\vec{\mu}_s^{\text{K(K}' )}}{dx} + \frac{v_d}{D_s} \vec{\mu}_s^{\text{K(K}' )} \right), \quad (\text{S10})$$

where we use  $R_{\text{sq}} = 1 \text{ k}\Omega$ , and  $W_{\text{gr}} = 0.5 \mu\text{m}$ . At  $x = 0$ , we assume that  $I_{sy}^{\text{K}}(x = 0) = I_{sy}^{\text{K}'}(x = 0) = P_i/4$ , with  $P_i = 0.1$ . At  $x = W_{\text{TMD}} = 5 \mu\text{m}$ , we assume that  $I_{sy}^{\text{K}}(x = W_{\text{TMD}}) = I_{sy}^{\text{K}'}(x = W_{\text{TMD}}) = 0$ . In the weak SOC regime, the spin accumulation ( $\mu_{sy} = \mu_{sy}^{\text{K}} + \mu_{sy}^{\text{K}'}$ ) decays exponentially and can be written using

$$\mu_{sy} = A \exp(x/\lambda_s) + B \exp(-x/\lambda_s), \quad (\text{S11})$$

where  $\lambda_s = \sqrt{D_s \tau_s}$ .

$$A = \frac{eP_i R_{\text{sq}} \lambda_s}{2W_{\text{gr}}} \frac{1}{1 - \exp(2W_{\text{TMD}}/\lambda_s)}, \quad (\text{S12})$$

and

$$B = A \exp(2W_{\text{TMD}}/\lambda_s) \quad (\text{S13})$$

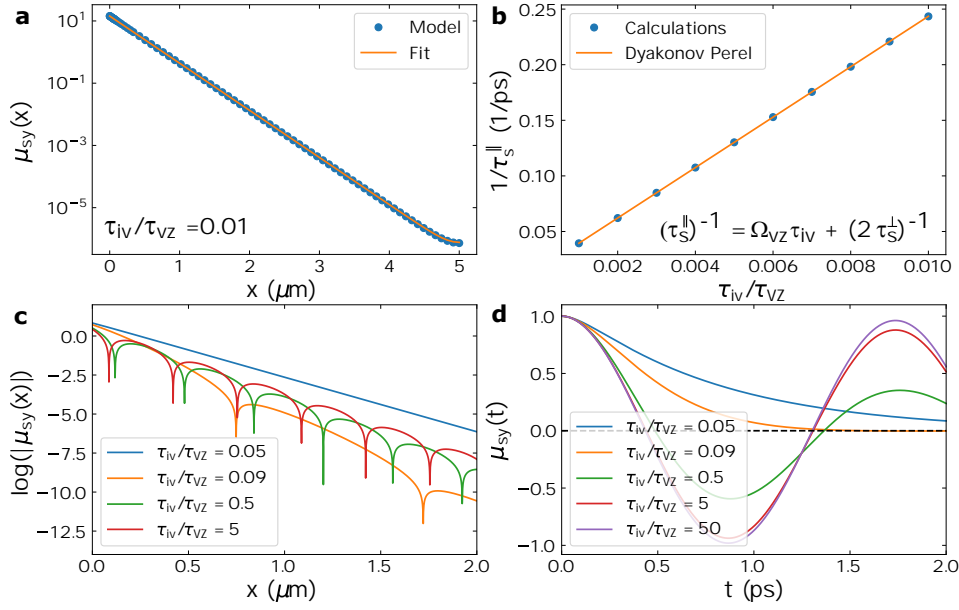


Figure S13. Output results of the two-valley model at  $I_{DC} = 0$ . (a)  $x$ -dependence of  $\mu_{sy}$  obtained from our model and its fit to Eq. S11. (b) In-plane spin relaxation rate as a function of  $\tau_{iv}$  in the weak SOC regime. (c) In-plane spin accumulation as a function of  $x$  for different values of  $\tau_{iv}$ . (d) In-plane spin accumulation as a function of time after an initial pulse at time  $t = 0$  for different values of  $\tau_{iv}$ .

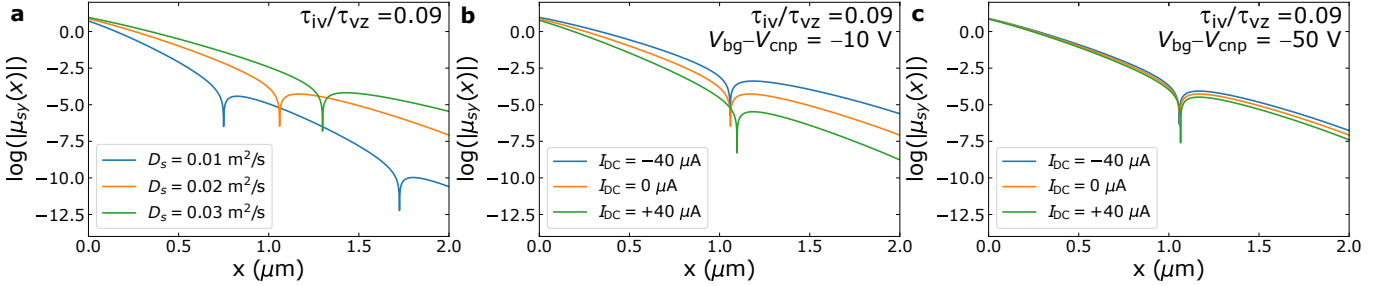


Figure S14. Effect of changing  $D_s$  and  $n$  on  $\mu_{sy}$ . (a)  $\mu_{sy}$  vs  $x$  at  $I_{DC} = 0$  and  $D_s = 0.01, 0.02,$  and  $0.03 \text{ m}^2/\text{s}$ .  $\mu_{sy}$  vs  $x$  at  $I_{DC} = -40, 0,$  and  $40 \mu\text{A}$  for  $\tau_{iv} = 0.09\tau_{vz}$ ,  $D_s = 0.02 \text{ m}^2/\text{s}$  and (b) for  $V_{bg} - V_{cnp} = -10 \text{ V}$  and (c) for  $V_{bg} - V_{cnp} = -50 \text{ V}$ .

are obtained from the boundary conditions for  $I_s^{K(K')}$ . To determine the effective spin lifetime, we fit the results from the two-valley model to Eq. S11 with  $\lambda_s$  as the only fitting parameter (see Fig. S13a).  $\tau_s$  is obtained using  $\tau_s = \lambda_s^2/D_s$ . Next, we plot the in-plane spin relaxation rate ( $1/\tau_s^{\parallel}$ ) as a function of  $\tau_{iv}$ , which we have normalized to  $\tau_{vz}$ . Figure S13b shows that  $1/\tau_s^{\parallel}$  is linear with respect to  $\tau_{iv}$ , as expected in the weak SOC regime. The orange line in Fig. S13b is a linear fit  $\tau_s^{\parallel -1} = C\tau_{iv} + D$ , where  $C = 3.262 \times 10^{24} \pm 6 \times 10^{20} \text{ s}^{-2}$  and  $D = 1.671 \times 10^{10} \pm 1 \times 10^7 \text{ s}^{-1}$  are the fitting coefficients. The inset text is the spin relaxation rate in the weak SOC (Dyakonov-Perel) regime [23]. We confirm the consistency of our model using that  $C = \Omega_{VZ}^2$  and  $D = (2\tau_s^{\perp})^{-1}$  and obtain  $\tau_s^{\perp} = 29.9 \pm 0.04 \text{ ps}$  and  $\Omega_{VZ} = (1.806 \times 10^{12} \pm 2 \times 10^8) \text{ s}^{-1}$ . These results agree well with the input parameters shown in Table II.

### Strong SOC regime

Once we have confirmed that our model works as expected in the weak SOC regime, we look at the strong SOC regime. For this purpose, we calculated  $\mu_{sy}(x)$  for  $0.05 < \tau_{iv}/\tau_{vz} < 5$  (see Fig. S13c). We observe that, for  $\tau_{iv}/\tau_{vz} = 0.05$ ,  $\mu_{sy}(x)$  does not change sign for  $0 < x < 2 \mu\text{m}$ . In contrast, for  $0.09 < \tau_{iv}/\tau_{vz} < 5$ ,  $\mu_{sy}(x)$  oscillates with  $x$  at a frequency that depends on  $\tau_{iv}$ . To understand if the change in the oscillation length comes from a change in the precession frequency around the SOFs or just a change in the spin lifetime, we have calculated  $\mu_{sy}(t)$  by assuming

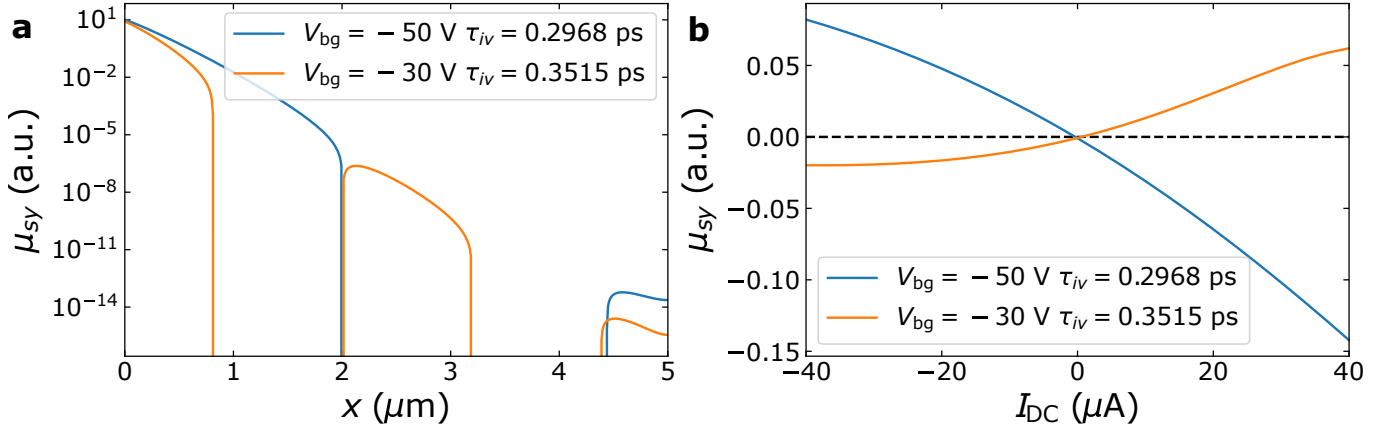


Figure S15.  $\mu_{sy}$  sign change with  $I_{DC}$  at different  $V_{bg}$ . (a)  $\mu_{sy}$  as a function of  $x$  at  $I_{DC}=0$  and (b) as a function of  $I_{DC}$  for  $V_{bg} = -30$  and  $-50$  V.

homogeneous spin injection ( $\frac{d^2 \bar{\mu}_s^{K(K')}}{dx^2} = \frac{d\bar{\mu}_s^{K(K')}}{dx} = 0$ ) at all times, and  $\mu_{sy}(t=0) = 1$ . Then we calculate  $\mu_{sy}(t)$  using Eqs. S7 and S8 and integrating them as ordinary differential equations with the input parameters shown in Table II. The results from this operation for  $0.05 < \tau_{iv}/\tau_{VZ} < 50$  are shown in Fig. S13d. We observe that, for  $\tau_{iv}/\tau_{VZ} = 0.05$  and  $0.09$ , there are no clear oscillations. For  $\tau_{iv}/\tau_{VZ} = 0.09$  the reason for this low signal is the fast decay of  $\mu_{sy}(t)$ , that we attribute to strong Dyakonov-Perel dephasing. In contrast, for  $0.5 < \tau_{iv}/\tau_{VZ} < 50$ , we see clear oscillations at a frequency that changes with  $\tau_{iv}$  at  $0.5 < \tau_{iv}/\tau_{VZ} < 50$ . As expected from the fact that the spins can complete several rotations between intervalley scattering events, for  $\tau_{iv}/\tau_{VZ}=50$  the frequency is the same as for  $\tau_{iv}/\tau_{VZ}=5$  and the only difference between these curves is that the former has a slightly slower decay.

To disentangle the origin of the sign change of the in-plane spin signal with  $V_{bg}$  reported in the main manuscript, one has to consider the different parameters which are changing with  $V_{bg}$ . These parameters are  $\tau_{iv}$ ,  $D_s$ ,  $n$  and  $\tau_s^\perp$ . The role of  $\tau_{iv}$  is shown in Fig. S13c.  $D_s$  changes the spin diffusion time (Fig. S14a),  $n$  modulates the effect of drift via  $v_d = I_{DC}/(W_{gr}ne)$ , and  $\tau_s^\perp$  gives rise to additional spin relaxation. We found that  $\tau_s^\perp$  does not modify  $\mu_{sy}(x)$  significantly unless the change in  $\tau_s^\perp$  is dramatic (from 5 to 60 ps), at odds with experimental results [25]. In contrast, as shown in Fig. S14a,  $D_s$  has a very strong influence on  $\mu_{sy}$  and is the most likely cause of the observed sign change with  $V_{bg}$ . Changing  $V_{bg}$  ( $n$ ) while keeping the other parameters fixed leads to the modification of the effect of drift, as shown in Fig. S14b and S14c and expected from the fact that  $v_d = I_{DC}/(W_{gr}en)$ . Accordingly,  $d\Delta R_{nl}/dI_{DC}$  is expected to change magnitude with  $n$  but not sign, as observed in the data.

The conclusion from this section is that the sign reversal of  $\Delta R_{nl}$  with  $V_{bg}$  and  $I_{DC} \neq 0$  is most likely caused by the change in  $D_s$ , which we obtain here using  $D_c$ . However, we cannot discard a change of  $\tau_{iv}$  with  $V_{bg}$ , which can also lead to the sign reversal of  $\Delta R_{nl}$ .

#### $I_{DC}$ -dependence of $\Delta R_{nl}$ .

Here we discuss the measured  $I_{DC}$ -dependence of  $\Delta R_{nl}$  in terms of our two-valley model. The most relevant feature of the data displayed in Figs. S6 to S9 is that  $\Delta R_{nl}$  changes sign near  $I_{DC}=0$ . This result is surprising at a first glance, since it contrasts with the spin drift experiments shown in the pristine graphene region (Section and Refs. 46 and 47). In this section, we show that the  $\Delta R_{nl}$  vs  $I_{DC}$  results measured across the TMD-covered graphene region are compatible with the model described by Equations S7-S9. For this purpose, we evaluate the spin accumulation at  $x = 2$   $\mu\text{m}$  as a function of  $I_{DC}$ . The outcome of this calculation, using the parameters from Table II, is shown in Fig. S15.

By tuning  $\tau_{iv}$ , it is possible to calibrate the position where the sign reversal of  $\mu_{sy}$  occurs and bring it to  $x = 2$   $\mu\text{m}$  (see Fig. S15a). In this case, a small positive (negative)  $I_{DC}$  can increase (decrease) the spin transport time and lead to a positive (negative)  $\Delta R_{nl}$  as reported here for  $V_{bg} = -30$  V and viceversa for  $V_{bg} = -50$  V (see Fig. S15). Note that, even though the sign reversal of  $\Delta R_{nl}$  with  $I_{DC}$  is compatible with the model, it occurs only for specific values of  $\tau_{iv}$ , which correspond to well defined spin precession frequencies. This is not necessarily the case for all values of  $V_{bg}$  so we would expect that, at other  $V_{bg}$ ,  $\Delta R_{nl}$  may be sizeable for  $I_{DC}=0$ , contrary to what is observed experimentally.

The results from Fig. S15 show that the magnitude of  $\Delta R_{nl}$  can increase when applying a positive and a negative

$I_{\text{DC}}$ , a feature which is not possible in the weak SOC regime. Note that the simulation does not include the effect of drift in the pristine graphene region that is expected to enhance the signal for negative  $I_{\text{DC}}$  and decrease the signal for positive  $I_{\text{DC}}$ .

We can list different features of the  $I_{\text{DC}}$  and  $V_{\text{bg}}$ -dependence of  $\Delta R_{\text{nl}}$  that strongly indicate that the measured dependence is inherent to the spin transport across the WSe<sub>2</sub>-covered region and not caused by a spurious effect from the spin drift measurement setup:

- The  $I_{\text{DC}}$ -dependence of  $\Delta R_{\text{nl}}$  at the pristine graphene region shows the expected trend for graphene (Section and Refs. 46 and 47). This means that the electronic setup, that is described in Section , is well calibrated to separate  $I_{\text{DC}}$  from  $I_{\delta}$ .
- The sign change of  $\Delta R_{\text{nl}}$  with  $I_{\text{DC}}$  does not occur at all  $V_{\text{bg}}$  values. For  $V_{\text{bg}} = -8$  V (Figs. S6c and S6g),  $\Delta R_{\text{nl}}$  is positive for both positive and negative  $I_{\text{DC}}$  and, for  $V_{\text{bg}} = -40$  V (Figs. S6b and S6e), a measurable spin signal is only observed for positive  $I_{\text{DC}}$ . Such dependence cannot occur in the weak SOC regime but is expected from the model described by Equations S7-S9.
- $\Delta R_{\text{nl}}$  changes sign multiple times when sweeping  $V_{\text{bg}}$  at fixed  $I_{\text{DC}}$  (Fig. 3d of the main manuscript). Hence, it is unlikely that the sign change is due to a simple modification of the charge current path with  $V_{\text{bg}}$ , as  $R_{\text{sq}}$  in both the pristine and WSe<sub>2</sub>-covered graphene regions have very similar  $V_{\text{bg}}$ -dependences (Fig. S3).
- The spin precession data shown in Figs. S7 and S9 shows that  $\Delta R_{\text{nl}}$  at  $B_x \approx \pm 0.1$  T, which corresponds to the shoulders where the spins travel across the WSe<sub>2</sub>-covered region out-of-plane, does not change sign with  $I_{\text{DC}}$  or  $V_{\text{bg}}$ . This is consistent with the fact that out-of-plane spins are not affected by the valley-Zeeman SOFs.

Finally, we note that, unlike that of Ref. 27, our model does not represent a fully relativistic description of the problem and may not be able to fully predict the expected dependencies of  $\Delta R_{\text{nl}}$ .

### Influence of the charged impurities on spin transport in the strong SOC regime

In the weak SOC regime, charge impurities were shown not to affect spin relaxation in graphene while having a significant influence on the electron mobility [61]. In contrast, in the strong SOC regime, the spin precession angles depend on the spin diffusion/drift time, that is dictated by charge transport, and  $\tau_{\text{iv}}$  (see Figs. S13c and S13d). Thus, the charge traps at the interface between BLG and WSe<sub>2</sub> may play a role in the backgate dependence of the spin signal. Even though this contribution is already included in the mobility and contributes to the diffusivity, it cannot be separated from other mechanisms limiting the mobility in our devices.  $\tau_{\text{iv}}$  is not affected by charge impurities because Coulomb interactions have a long range.

### TIGHT BINDING CALCULATIONS

The band structure shown in Figs. 2e and 2f of the main manuscript has been obtained using the Hamiltonian described in Ref. 30. Here, for the sake of completeness, we show the Hamiltonian, that has two different components:

$$H_{\text{orb}} = \begin{pmatrix} \Delta + V & \gamma_0 f(k) & \gamma_4 f^*(k) & \gamma_1 \\ \gamma_0 f^*(k) & V & \gamma_3 f(k) & \gamma_4 f^*(k) \\ \gamma_4 f(k) & \gamma_3 f^*(k) & -V & \gamma_0 f(k) \\ \gamma_1 & \gamma_4 f(k) & \gamma_0 f^*(k) & \Delta - V \end{pmatrix} \otimes s_0,$$

accounting for the orbital effects and

$$H_{\text{SOC}} + H_{\text{R}} = \begin{pmatrix} \tau \lambda_{\text{I}}^{\text{A1}} s_z & i(\lambda_0 + 2\lambda_{\text{R}}) s_{\text{I}}^{\text{I}} & 0 & 0 \\ -i(\lambda_0 + 2\lambda_{\text{R}}) s_{\text{I}}^{\text{I}} & -\tau \lambda_{\text{I}}^{\text{B1}} s_z & 0 & 0 \\ 0 & 0 & \tau \lambda_{\text{I}}^{\text{A2}} s_z & -i(\lambda_0 - 2\lambda_{\text{R}}) s_{\text{I}}^{\text{I}} \\ 0 & 0 & i(\lambda_0 - 2\lambda_{\text{R}}) s_{\text{I}}^{\text{I}} & -\tau \lambda_{\text{I}}^{\text{B2}} s_z \end{pmatrix},$$

accounting for the spin-orbital effects. The latter is written on the basis elements:  $|C_{\text{A1}}, \uparrow\rangle$ ,  $|C_{\text{A1}}, \downarrow\rangle$ ,  $|C_{\text{B1}}, \uparrow\rangle$ ,  $|C_{\text{B1}}, \downarrow\rangle$ ,  $|C_{\text{A2}}, \uparrow\rangle$ ,  $|C_{\text{A2}}, \downarrow\rangle$ ,  $|C_{\text{B2}}, \uparrow\rangle$ , and  $|C_{\text{B2}}, \downarrow\rangle$ , where A1(2) and B1(2) correspond to the A and B sites on the bottom(top) layer, respectively.  $\gamma_{0,1,3,4}$  are the tight-binding parameters[30] (Table III) and  $f(k) = \exp\left(\frac{ik_y a}{\sqrt{3}}\right) +$

TABLE III. Tight binding parameters in eV.

$\gamma_0$	$\gamma_1$	$\gamma_3$	$\gamma_4$	$\Delta$	$V$
2.453	0.372	-0.27	-0.162	$-10.208 \times 10^{-3}$	0
$\lambda_I^{A1}$	$\lambda_I^{A2}$	$\lambda_I^{B1}$	$\lambda_I^{B2}$	$\lambda_0$	$\lambda_R$
0	$1.07 \times 10^{-3}$	0	$-1.179 \times 10^{-3}$	0	0

$2 \exp\left(-\frac{ik_y a}{2\sqrt{3}}\right) \cos\left(\frac{k_x a}{2}\right)$  the nearest-neighbour structural function where  $k = (k_x, k_y)$  is a reciprocal space vector and  $a = 0.246$  nm the lattice constant.  $s_{\pm}^{\tau} = (s_x \pm i\tau s_y)/2$  where  $\tau = +(-)1$  in valley K(K'). The band structure of Fig. 2e has been calculated by finding the eigenvalues and eigenvectors of the Hamiltonian  $H_{\text{tb}} = H_{\text{orb}} + H_{\text{SOC}} + H_{\text{R}}$  for valley K.

### EFFECT OF A PERPENDICULAR ELECTRIC FIELD ON THE SPIN TEXTURE OF BILAYER GRAPHENE

When its inversion symmetry is broken by a perpendicular electric field, bilayer graphene opens a gap and displays an out-of-plane spin splitting near the charge neutrality point that has the same symmetry as the valley-Zeeman SOC [62]. However, the magnitude of this SOC is  $12 \mu\text{eV}$ , leading to a precession period  $\tau_{\text{so}}=172$  ps. Such long spin precession period, which increases quickly as the carrier density is tuned far from the charge neutrality point, is already significantly longer than typical intervalley scattering times in bilayer graphene on  $\text{SiO}_2$ , that are in the range of 10 ps [37]. Accordingly, recent experimental works have shown that spin transport in bilayer graphene remains in the weak SOC regime, with long spin lifetimes in the ns range, even when a perpendicular electric field is present near the charge neutrality point [41, 59]. We conclude that the effect of the perpendicular electric field alone (without the SOC induced by the  $\text{WSe}_2$ ) cannot account for the observed spin precession in bilayer graphene.